STUDY FOR THE EXPERIMENTAL ANALYSIS OF NEUTRON TRANSPORT AND TRITIUM BREEDING PERFORMANCE INSIDE FUSION REACTOR BLANKET

YASUYUKI OGINO

Contents

ABSTRACT

Several countries are less abundant about energy resources than others, and they are dependent on importing energy resources. Since it is financially and politically critical, they are focusing on finding solutions for such energy problems through the innovations. Fusion reactor is one of the promising sustainable energy resources and would be utilised as the energy source capable of converting thermal heat through a blanket system. The blanket system is one of the important components around the fusion reactor to make fusion device a reactor. Although techniques for the control of plasma on fusion fields has been developed through experiments employing plasma devices, blanket system has not been sufficiently developed. Blanket system mainly has three roles: to transfer the heat generated from the attenuation of neutrons; to generate fuel tritium for the self-sufficient operation of fusion reactor through the transmutation of lithium contained in the breeding materials; to shield radiations not to leak outside. Although several fusion devices like ITER are planned to install the neutron activation system using pneumatic tubes, this system detect and measure neutrons only at one position by one system. Neutrons and bred tritium are broadly distributed inside the blanket module, and it is even important to evaluate them spatially. In this thesis, I focused on the neutron transport and methodology of measuring neutrons inside the blanket. Neutron irradiation experiments and simulations were performed and compared each other to propose and verify the measuring methods.

Chapter 1 describes the background based on the above and determine the purpose of this thesis. By introducing the background of energy problems in Japan and on the whole world, the approaches of the fusion reactor for solving these problems are emphasized. Then, requirements of neutronics experiments for the development of blanket systems are introduced, and current issues of measurement of neutron and tritium are summarized. After these introductions, the purpose of this thesis is determined.

Chapter 2 proposes a novel method to measure spatial neutron distribution through an activation analysis and verifies the preliminary resolution of the spatial measurement. A 2-dimensional radiation dosimeter called an imaging plate and material foils or wires were employed for the activation analysis. Materials were installed inside a mock-up composed of

polyethylene and were irradiated by a discharge-type cylindrical deuterium-deuterium neutron source. Neutron production rate was measured by a ^{3}He gas-filled detector and was about 1 x 10^{5} n/sec. Measured values by the imaging plate were converted into the total number of decays of activation foils by the calibration results of a γ-ray standardised source. These values were compared with the simulations of neutron transport by MCNP and activation analysis by DCHAIN-SP. These results propose that the method using the imaging plate and material foils was feasible to apply to the measurement of neutron spatial distribution inside the blanket mock-up.

Chapter 3 proposes a method to measure neutron fluences by specific energy regions of thermal, epi-thermal, and fast neutrons. A collaboration of different material foils was employed for this method. Based on the differences between (n,γ) reaction cross sections, materials were installed inside mock-ups composed of polyethylene and graphite, and activated by the irradiation of neutrons differently. Employing these differences of total number of reactions, activation analyses were performed and compared with the simulated results obtained by neutron transport code and activation analysis code.

Integrating Chapter 2 and Chapter 3, novel methods of measuring spatial neutron distribution divided into specific energy regions were proposed. Employing the imaging plate and material foils, neutron fluxes were obtained divided into thermal and epi-thermal neutrons regarding the reaction cross section of each material.

Chapter 4 introduces a preparation result to measure neutron spatial distribution with specific energy regions inside a blanket mock-up using deuterium-tritium neutron source. For the consideration of measuring neutrons, the geometric design of the mock-up and the combination of material foils were determined through simulations of neutron transport. For employing the imaging plate, time transitions for the activation analyses were considered by each material foils. Installing material foils inside the mock-up, neutron fluxes were obtained by energy regions and time transitions of using the imaging plate and the combination of materials were simulated and calculated through the activation analysis. Tritium production inside the mock-up was also calculated, and dominant region of neutron energy was different among the breeding layers. Selected material foils were confirmed to be employed for the measurement of each energy region of neutrons.

Based on these results, the neutron distribution divided into energy regions is feasible to be measured inside the blanket, and this method is also feasible to be applied for measuring tritium production. For the future study, the actual experiment irradiating DT neutrons is required, and the accuracy of the measurement value obtained by the imaging plate is required to be improved.

1. Introduction

1.1 Energy resource and carbon neutrality

Several countries, including Japan, are less abundant about energy resources than others. They are dependent on importing energy resources (e.g., coal, petroleum, LNG of fossil fuels), which has been financially and politically the critical issue. They are focusing on finding solutions for such energy problems through the development of innovative, efficient, and ecological methods.

European countries have promoted to shift from fossil fuels to renewable energies as they are conscious to the balanced energy mix and try to stop using fossil fuels for generating electricity. On the other hand, since some countries sell energy to neighbouring countries as electricity because of the abundance of resources, total balance of energy mix are required for each unit of EU, ASEAN, and Asia for example, to be considered. The affair of promotion of energy resources gradually changes as nuclear power begins to be regarded as renewable energy again by reflecting the current trends of restriction of carbon emissions in the EU.

A nuclear power plant is one of the solutions for energy problems, however, it remains serious problems: an initial resource of uranium as fission plant is imported; though used nuclear fuels called low- and high-level radioactive waste need to dispose properly, there remains several issues. Based on the policy for the solution of the energy problem in Japan, sustainable energy resources (mainly the solar power) are determined to be promoted along a milestone for the near future of 2030 and 2050. Since sustainable energy resources are restricted by conditions of climate, geographical features, and other factors, it is difficult to choose sustainable energy resource as the base-load energy in Japan even after the severe accident in 2011. The baseload power in Japan will be still highly possible to depend on thermal power or nuclear power plants.

Nuclear fusion reactor has been parallelly developed with nuclear fission. There are fundamentally and technically important differences between fusion and fission: mass number of mother nuclide increases after fusion reaction; released energy per reaction by familiar fusion reaction is lower than fission reaction, and there is no chain reaction itself after fusion

reaction (as shown in Eq. (1) and (2), for example); in contrast to the control to shut down for fission reactor, the control for a confinement to hold a plasma for maintaining the fusion reaction enough for a targeted power gain; fusion reactor requires more efficient components to harness energy as thermal energy or electricity.

$$\mathrm{D} + \mathrm{T} \rightarrow {}^{4}\mathrm{He} + \mathrm{n} + 17.1\ \mathrm{MeV} \quad (1)$$

$${}^{235}\mathrm{U} + \mathrm{n} \rightarrow {}^{236}\mathrm{U} \rightarrow {}^{89}\mathrm{Kr} + {}^{144}\mathrm{Ba} + 3\mathrm{n} + 177\ \mathrm{MeV} \quad (2)$$

Though techniques for the operation of a nuclear power plant have been matured, there are still issues for the safety and disposal of both high- and low-level radioactive wastes.

For the achievement of suppressing warming within 2 or 1.5 degrees Celsius, there is a critical restriction of carbon emissions. More than 100 countries pledge to cut greenhouse gas emissions by 2025–2030 at Paris Agreement in 2015 and achieve carbon neutrality on earth. This agreement

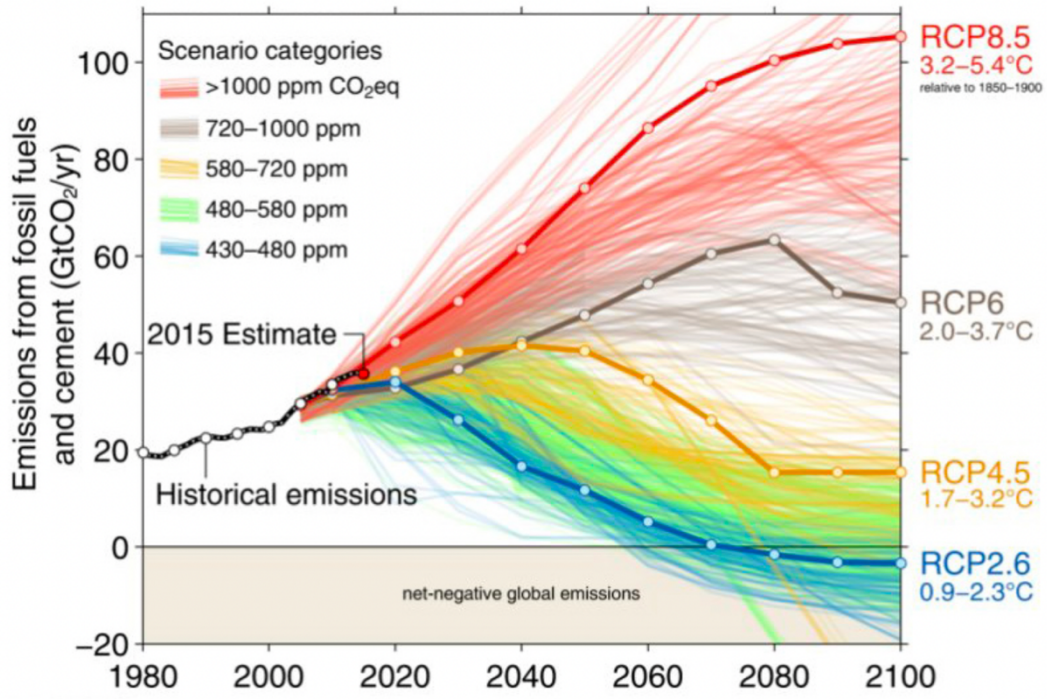

Fig. 1–1 Estimated transitions of carbon emissions from fossil fuels and cement based on the policies of RCP2.6, 4.5, 6, and 8.5 [1]

sets their targets individually, however, they have continued considering the solution with sustainability and mobility for humankinds.

Considering the "representative concentration pathways" (RCP), each transition of total CO_2 emissions was estimated. One of estimations shown in Fig. 1–1 indicates that we would suppress the warming between 0.9–2.3 degrees of RCP 2.6 by carbon neutrality by around 2070 [1]. Another estimation shown in Fig. 1–2 shows transitions about representatives of warming limits[2]. The severest case of warming below 1.5 Kelvin requires to accomplish carbon neutrality earlier than 2050 for any optimistic and pessimistic cases. It is also estimated that the fast mitigation from previous policies of emissions to low emission pathways such as RCP 2.6 is much better than slow mitigation because of carbon budget. Carbon budget which indicates the rest of allowable emissions to a goal of carbon neutrality affects future emissions. Promoting fast mitigations leads low carbon negatives after carbon neutrality; otherwise, severely forces high carbon negatives.

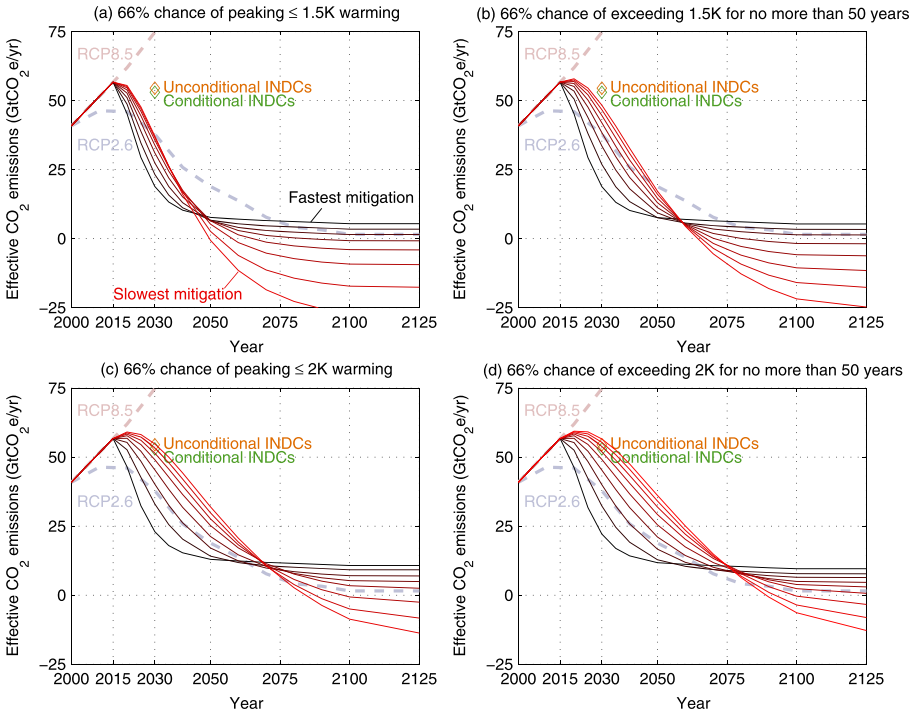

Fig. 1–2 Estimated pathways of CO_2 emissions with several actions and targets of warming limits [2]

1.2 Fusion reactor and blanket

Fusion reactor would be utilised as the energy source capable of converting thermal heat through the blanket system which is one of the components around the fusion reactor. Previous studies on fusion fields, characteristics of plasma has been experimented employing plasma devices. For obtaining high performances of plasma parameters, a lot of types of plasma devices were proposed and torus-type devices has been constructed (originally since 1950s). Torus devices realize to confine plasma with longer periods, high densities of ions, electrons, and α-particles, and keep high temperatures of ions and electrons.

Fusion reactor which employs nuclear fusion reactions with deuterium, tritium, or other light mass elements has been promoted as sustainable, eco-friendly, and self-sufficient power resources since the 1950s. Currently, conceptual fusion approaches have been proposed, and several concepts, for example tokamak, stellarator, helical, spherical tokamak, or laser have been experimented by actual experimental plasma devices. After proposing torus-shaped reactors, both experimental fusion devices and conceptual design of fusion reactors have become on large scale.

Previous fusion studies have been developed mainly funded from the government, and the new trends of development focusing on commercial use

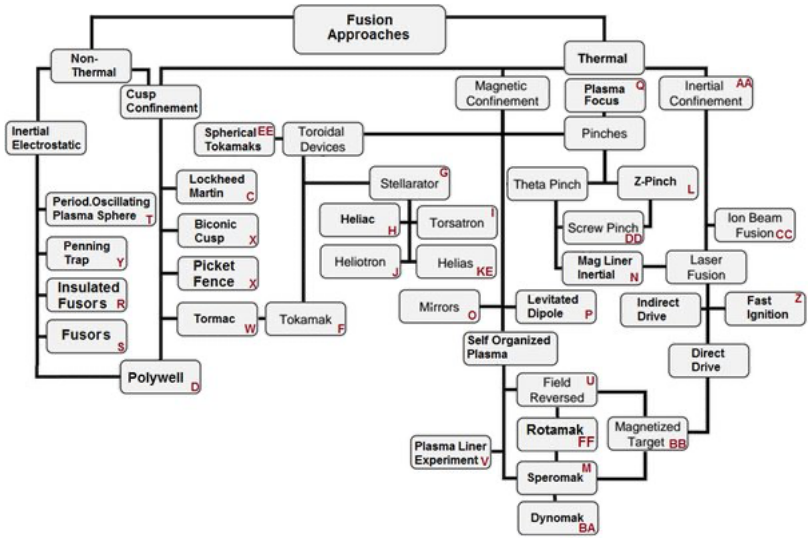

Fig. 1–3 Fusion approaches classified into similar types or derivations [5]

are trying to fabricate pilot plants in 2030–2040s which is based on tokamak, laser, Z pinch[3], spherical tokamak[4], and such relatively small types compared to previous types, shown in Fig. 1–3[5].

Fusion power is generally evaluated through the ratio of output to input defined as the symbol of capital Q. Q value directly represents the performance of the fusion reactor, and this value is set to the criteria of each fusion device and future design of fusion reactors. In previous studies, Joint European Torus (JET) in the UK was achieved almost at Q = 0.67, and JT-60 in Japan was accomplished to reach more than unity (Q = 1.25)[6]. In the case of ITER, the target of Q value was set to more than 5. Fusion power depends on essential parameters of plasma which is determined by the phase of design (mainly conceptual design), and the efficiency of conversion depends on the performance of the blanket, heat exchanger and other components around them.

The conversion from fusion power into thermal energy is occurred by collision between neutrons and the first wall or the divertor wall, and nuclear reactions inside the blanket. Energy load of collisions between neutrons and first wall is defined as 'neutron wall load' which is designed to be 0.56–0.78 MW/m^2 for ITER. For the design of a DEMO fusion reactor with 1.35 GW of a fusion power, the peak neutron wall load on inboard and outboard blankets were calculated to be 0.95 and 1.50 MW/m^2[7]. Irradiated neutrons are reacted with blanket materials and generated radiations are converted into thermal energy through collisions with other materials. Energy depositions by radiations were calculated through the factor of "kinetic energy released in matter" (KERMA). The KERMA factor depends on the energy of radiations and irradiated materials, and this was considered for the application of the design of fusion blankets.

Based on the above, a fusion reactor is planned to determine parameters from the shape, size of plasma, endurance of materials, and fusion power output. Since fusion blankets should be designed properly corresponding to these parameters, there are many types of blankets proposed through the simulations and experiments.

Blanket (or blanket system) is one of the important components in the fusion reactor. The blanket has following rolls:

- to convert thermal energy from first walls and kinetic energy from neutrons into heat output and transfer them
- to breed tritium as fusion fuel for self-sufficiency
- to prevent the spread of radiations (neutrons, especially) following the "*as low as reasonably achievable*" principle (ALARA).

The blanket is composed of a functional material and a structural material[8]. The functional material is expected to work as production of tritium and multiplication of neutrons for improving tritium production, and the structural material is expected to work as the container for the functional material and coolant material.

For the functional materials, beryllium and lithium are promising candidates. Beryllium is employed as the neutron multiplier through (n,2n) reaction and attenuate neutrons through scattering reactions. As the candidate of beryllium inside the blanket, titanium beryllide and vanadium beryllide are candidates; pure beryllium is not suitable because of endurances for high temperature environment and chemical resistances. Lithium is employed as the tritium breeding material through (n,t) and (n,n't) reactions by lithium-6 and lithium-7, respectively. Since (n,t) reaction is easy to occur and its reaction generates nuclear heat, it is important or prerequisite to enrich lithium-6 as much as possible (generally enriched to 90 or 99 %) compared to the natural abundant of 7.5 %. (n,n't) reaction by lithium-7 , in contrast, absorb thermal energy, and (n,n't) reaction cross-section of lithium-7 has threshold energy. As the candidates of lithium are lithium titanates lithium silicates in recent studies. Both multipliers and breeders are manufactured to pebble shape which makes easy to manufacture, release heat and tritium. Multiplying neutrons by beryllium pebbles, the absolute number of neutrons are expected to increase, and it contributes the tritium production.

For the structural materials, several candidates has been proposed and mechanical, chemical, and radioactive characteristics have been experimented[9]. Most of the concepts are reduced-activation ferritic/martensitic (RAFM) steels, for example F82H, Eurofer, hiperfer, CLAM, and Rusfer. RAFM steel are suitable for mass production, and they are highly durable for radiations and activation compared to general steels because of the mixture of elements such as chromium and tungsten. The structural material also for coolant such as water with high pressure and

temperature, and gaseous helium with small amount of hydrogen for the isotopic exchange of tritium inside the functional materials[10].

The configuration of blanket has been developed through evaluations of mechanical properties of composed materials, chemical reactions between functional and structural materials, and performances of nuclear reactions.

In the previous studies, a WCCB (water cooled ceramic breeder) test blanket module was a box-shaped configuration installed in ITER[11] shown in Fig. 1–4.

When a breeding layer has been set thickness to some extent, the performance of tritium breeding varies from surface to middle because the absorption of thermal neutrons is occurred on the surface.

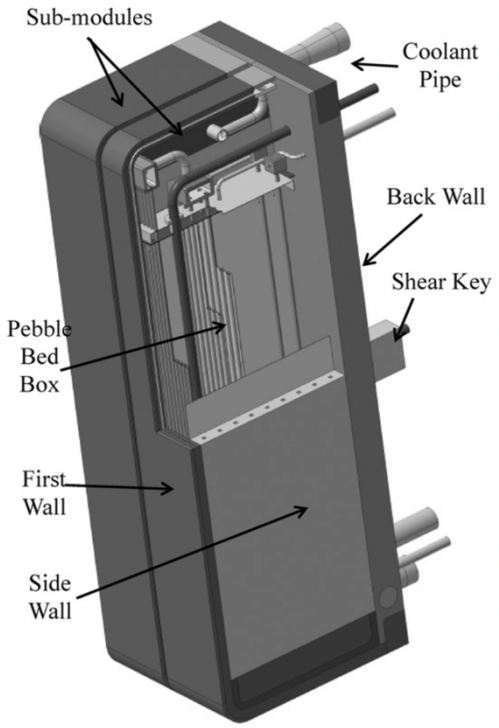

Fig. 1–4 The previous conceptual design of WCCB test blanket module installed in ITER: Pebbles were contained in the bed box and apart from each material [11]

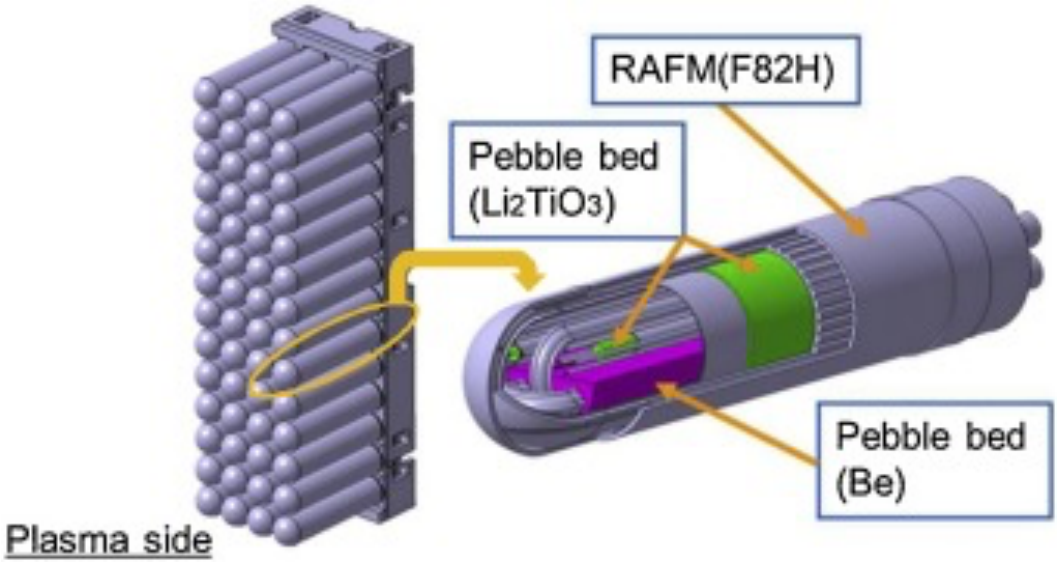

Fig. 1–5 Cylindrical model of WCCB test blanket module and its submodule [13]

Fig. 1–5 shows the current model of WCCB test blanket module installed on ITER[12], [13]. This concept is composed of a cylinder and a hemispherical head facing to the plasma, and tubes for coolant are introduced inside the module. Compared with the previous model, this shape has high resistances against coolant pressure, electromagnetic and heat load from plasma, and components for confinement.

Both tritium production and heat output are essential performance for a fusion reactor and there is a balance that the performance of tritium production is decreasing in the case of increasing the performance of heating and vice versa.

It is necessary for the fusion reactor to breed tritium inside the blanket. Required tritium breeding ratio (TBR) is more than unity or 1.05 with uncertainty considering factors of tritium inventory, numerical calculations, and measurements[14] for the whole blanket. In particular, the blanket is divided into modules and each TBR, called local TBR, is defined as considerations of an actual reactor. There are several ports for plasma heating devices of NBI and ECH, vacuum systems, divertors, and diagnostic probes. Since areas for these components were required, an effective area of the blanket is considered. According to the design of Japan DEMO reactor, coverage of the blanket is defined as approximately 91.8%. The required local TBR is at least 1.39 and estimated TBR is 1.16[15].

Heat output depends on the transport of thermal energy from the plasma to the blanket and the transferring performance of systems including the blanket and transferring pipes.

Tritium production is broadly distributed inside the Li layer of the blanket. In the case of mock-up experiments, tritium productions at several positions were simulated and measured by liquid scintillation counter which detects scintillation luminescence from β-rays of 18.6 keV at most. Ratio of tritium production steeply decreases inside the Li layer[16]–[18]. Considering the transfer of tritium with water coolant or helium coolant gas, it is essential for installing each coolant with effective positions.

1.3 Development of neutronics on fusion fields

A fusion reactor would be mainly composed of vacuum vessel, divertor, blanket, heat injector of neutral beam injection (NBI) port or electron cyclotron heating (ECH), maintenance probes and ports, magnetic field coils, bio shields, and many other components. The fusion reactor is asymmetric in both toroidal and poloidal directions, which suggests that the performance evaluation of fusion reactor requires the inhomogeneous simulation.

In addition, a lot of works about blanket mock-up experiments were reported. Neutronics experiments employing mock-ups were performed for the tritium breeding performance, the neutron multiplying effect, and the material benchmarking of neutron transport inside the mock-up. Several suggestions of tritium breeding, neutron multiplying, and structural materials were tested about chemical properties, radiation resistance as in-situ experiments. Employing these candidates of functional materials and structural materials, mock-up experiments were performed by accelerator-based neutron sources (e.g., FNS of JAEA (former JAERI), FNL of Tohoku University, OKTAVIAN of Osaka University for domestic, and RTNS-II [19] for U.S.). They still have developed and have promoted next steps

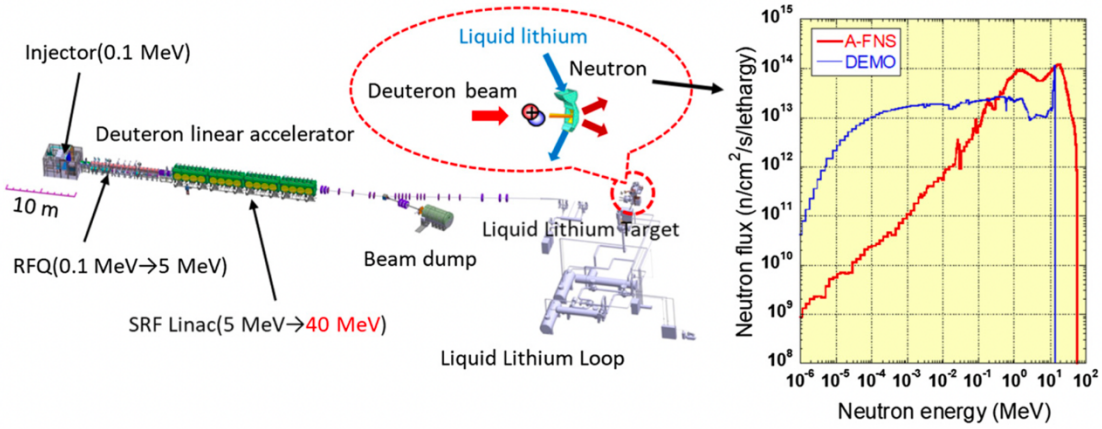

Fig. 1–6 Conceptual design of A-FNS and the calculated neutron spectrum compared with JA-DEMO [19]

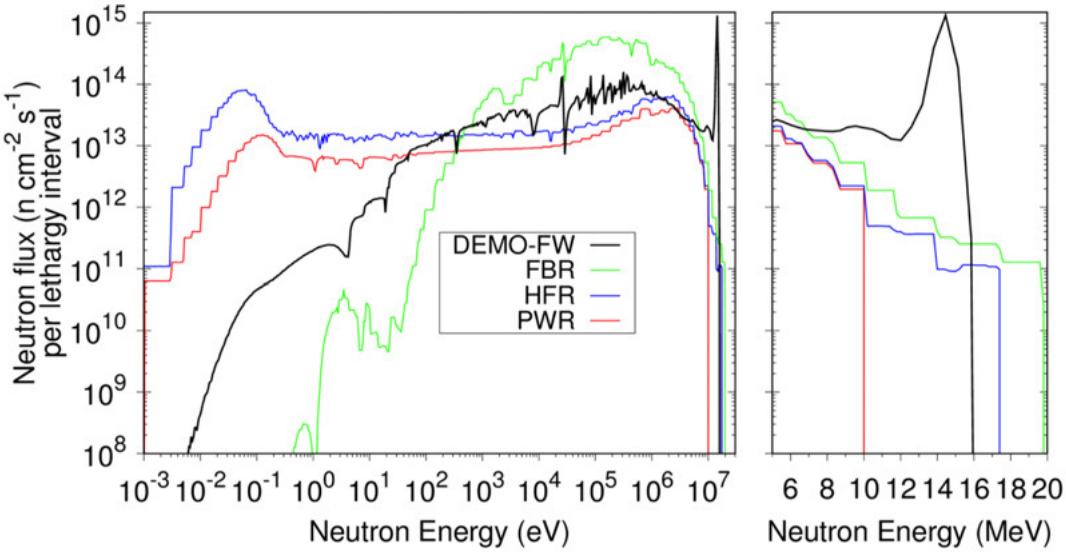

Fig. 1–7 Comparisons of neutron energy spectra with types of nuclear power plants and fusion DEMO reactor [24]

through a planned device of A-FNS (advanced-FNS), QST, Japan[20], [21] or a working device of FNG (Frascati neutron generator), ENEA, Italy[22], [23].

Fig. 1–7 shows the energy spectra of fusion DEMO reactor at the first wall and each type of nuclear power plant[24]. As shown in this figure, the neutron fluxes of thermal energy region are significantly different with nuclear types of HFR and PWR and breeding types of DEMO-FW and FBR. Neutron fluxes depend on the type of structures which includes the breeding layer or not. Fig. 1–8 shows the neutron spectra of neutron sources and fusion devices[25].

Main purposes of neutronics experiments for the application of the fusion reactor are followings; for the confirmation of applied materials exposed by radiations, evaluations of neutron fluxes particularly generated by D-T, D-D, and T-T fusion reactions, evaluations of nuclear reactions dominant for the fusion reactor (n,2n), (n,3n),… reactions by multipliers, (n,t) and (n,n't) reactions by breeders, and neutron absorption (capture) by (n,γ) reaction. Neutron production rate is generally measured using a micro-fission chamber or a He-3 (^{3}He) gas-filled proportional counter, a type of gas ionization detectors. The fission chamber which applies the fission reaction of fissile materials such as uranium (coated as $^{235}UO_2$ for the inner side of its electrode) is mainly employed as neutron counting monitor systems installed at nuclear plants, plasma devices, and other facilities with neutron production. Compared with non-coated chambers, the coating of fissile materials induces

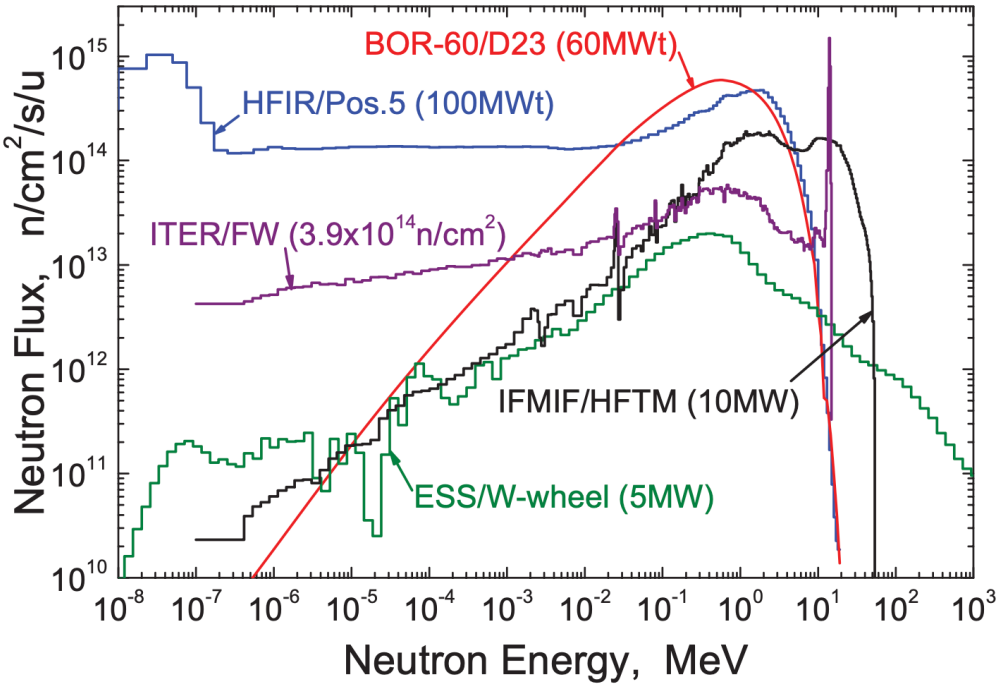

Fig. 1–8 Neutron energy spectra of neutron sources and fusion devices based on simulations [19]

ionization of argon gas inside by fission fragments and α-particle and contributes the improvement of detection efficiency and sensitivity. The fission chamber provides a wide dynamic range of 10^{10} and time resolution within 1 millisecond with combinations of operating modes (for the ITER grade)[26]. The ^{3}He gas-filled proportional counter is generally employed for relatively small-size devices. The ^{3}He counter provides a wide dynamic range and high sensitivity between thermal and fast neutrons. In the case of measuring the neutron energy spectrum, the time of flight (ToF) method is generally applied[27]. The ToF method is based on the mean free path (average distance) of a neutron. Though this method realises to obtain accurate neutron energy spectrum, there are requirements to make pulse operation or shutter closing of neutrons.

Although neutron measuring methods for specific characteristics such as energy spectrum and production rate have been developed for a long time, neutron measuring systems focused on fusion blankets has not been developed sufficiently. The neutron measuring method using activation foils plans to be installed for ITER with neutron activation system (NAS) which has been installed for previous devices on fission or fusion fields. The NAS aims for neutron diagnostics at some fixed points (inside TBM, around components)[28]. However, since there are neutrons and bred tritium

broadly distributed inside each blanket module, the method of measuring both spatial distribution and energy spectrum of neutron is required.

1.4 Summary of Chapter 1 and purpose of this thesis

Chapter 1 introduced the background of energy problems in Japan and on the whole world and the approaches of the fusion reactor for solving these problems. Then, requirements of neutronics experiments for the development of blanket systems were introduced, and current issues of measurement of neutron and tritium were summarized.

Chapter 2 introduces a novel method to measure spatial neutron distribution through an activation analysis. This method employs a 2-dimensional radiation dosimeter called an imaging plate and material foils and wires for the activation analysis. Materials were installed inside mock-ups composed of polyethylene and were irradiated by a discharge-type deuterium-deuterium neutron source.

Chapter 3 introduces a method to measure neutron fluences divided into specific energy regions of thermal, epi-thermal, and fast neutrons. This method employs a collaboration of different material foils. Based on the differences between (n,γ) reaction cross sections, materials were installed inside mock-ups composed of polyethylene and graphite, and activated by the irradiation of neutrons differently. Employing these differences of total number of reactions, activation analyses were performed and compared with the simulated results obtained by neutron transport code and activation analysis code.

Chapter 4 introduces a preparation result to measure neutron spatial distribution with specific energy regions inside a blanket mock-up using deuterium-tritium neutron source. For the consideration of measuring neutrons, the geometric design of the mock-up and the combination of material foils were determined through simulations of neutron transport. For employing the IP, time transitions for the activation analyses were considered by each material foils.

The purpose of this thesis is to establish a novel method of measuring spatial distribution and energy spectrum of neutrons inside the blanket mock-up. Both chapter 2 and 3 proposes the method to measure spatial distribution and energy, respectively. Chapter 4 is the preliminary simulation of an actual experiment of measuring neutrons using 14 MeV neutrons irradiated by a deuterium-tritium neutron source.

2. Measurement and analysis of neutron distribution using imaging plate and material foils/wires

2.1 Introduction

Since the performance of tritium breeding is not homogeneous inside the whole blanket of a fusion reactor, the fixed-point measurement applying the conventional methods using a pneumatic tube is insufficient for activation analyses. Current studies of the blanket design are proposed that a cylindrical or a boxed compartment is required for each module with simulations based on the precise model and time (particle histories of random generation) for calculation. Previous considerations of the DEMO fusion reactor blanket design were mainly based on the simulation results of neutron transport code and benchmarking results through the blanket mock-up experiments[29].

This chapter aims to establish a method measuring the spatial distribution of neutron fluxes and using activation foils and wires in a blanket module assembly. The radiations from the activated materials were measured by an imaging plate (IP). Advantages of employing the IP are:

1. able to obtain photo-stimulated luminescence (PSL) 2-dimensionally
2. reusable after erasing remaining data with intense light as shown in Fig. 2–1 and the right bottom of Fig. 3–3. In this work, the spatial distributions of neutron fluxes were measured with activation materials and the IP.
3. sensitive to α-, β-, and γ-rays. The sensitivity to β-rays is advantageous compared to other dosimeters.

The experimental results were compared with the simulation of neutron transport by MCNP. For the activation analysis, particle transport and activation analysis code of PHITS/DCHAIN-SP were employed in this work.

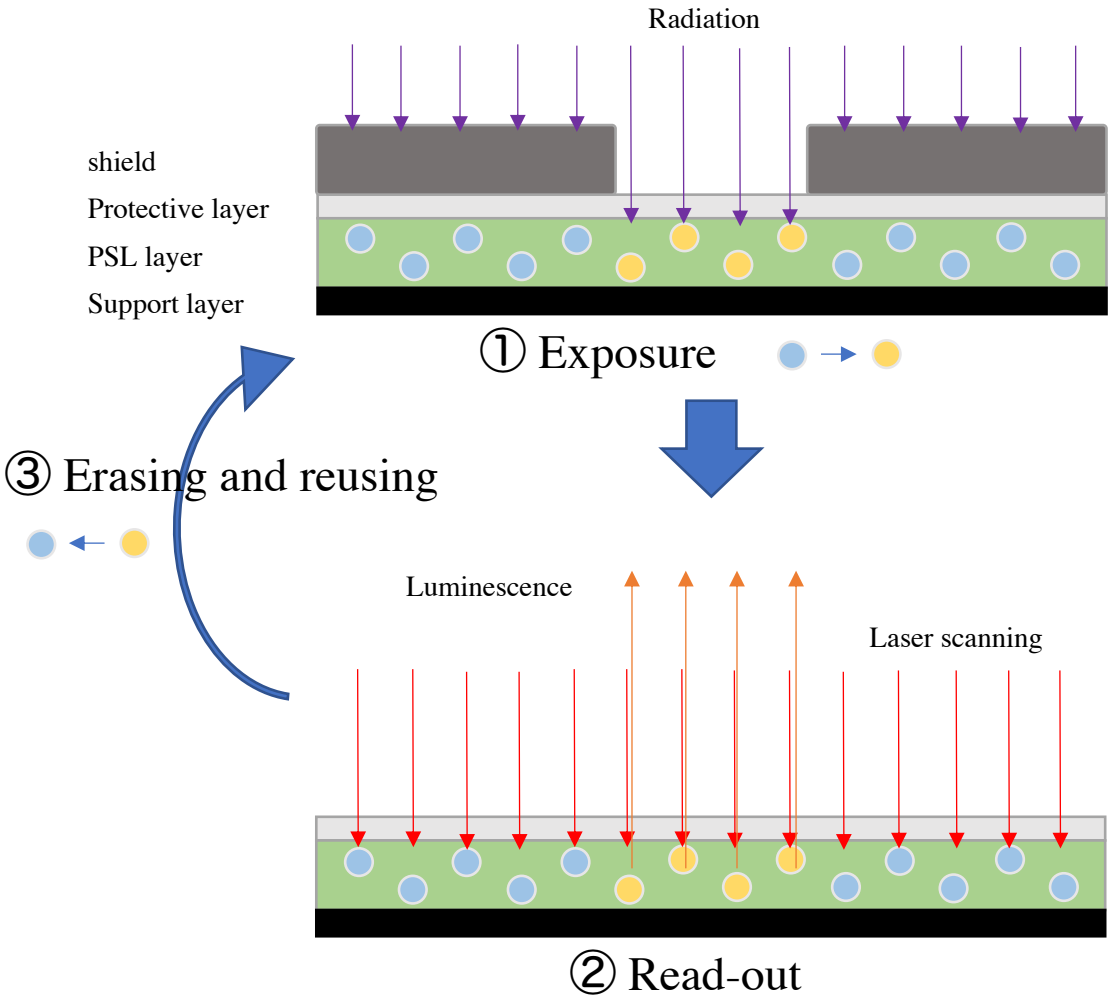

Fig. 2–1 Sequences for employing the IP: expose the radiation to the IP; read-out the cumulative data

2.2 Method

For the experiment of the measurement of neutron fluxes, the deuterium-deuterium (DD) discharge-type cylindrical fusion device was employed. This device generates monochromatic 2.45 MeV neutrons by DD fusion reactions[30], [31]. The glow plasma surrounded by the cylindrical cathode and two anodes, located at the edge of vacuum chamber, generates DD fusion neutron by applying high voltage. Current and voltage from power supply system were applied to 5 mA and 70 kV at most, in this work.

The average D_2 gas pressure was controlled to be 0.65–0.80 Pa in the cylindrical vacuum chamber during discharge.

The neutron production rate (NPR) was measured by a ^{3}He gas-filled counter. The ^{3}He counter was located neighbouring the vacuum chamber (shown in Fig. 2–9). The ^{3}He counter was calibrated with a spontaneous ^{252}Cf fission neutron source (its activity and NPR were 1.25 x 10^4 Bq and 1.47 x 10^3 n/s) whose averaged neutron energy of 2.3MeV is close to the neutrons (2.45 MeV) emitted from the DD fusion device. The ^{252}Cf source was put inside the cylindrical cathode during calibration, and the relation between the NPR and the number of counts from the ^{3}He counter was obtained.

An imaging plate (BAS-MS2025, Fujifilm) was employed to measure β-rays and γ-rays emitted by activation materials converted as value of PSL. The IP is composed of layers of a fine mixture of photo-stimulated luminescent materials ($BaBrF:Eu^{2+}$), ferrite and a flexible support made of plastic.

For the activation analysis, dysprosium (Dy), indium (In), and gold (Au) were employed as activation foils and wires. The thickness of every foil was 0.05 mm and the diameter of wires were 0.5 mm for each. The estimated reactions of these materials are below: ^{164}Dy reacts with thermal neutrons as $^{164}Dy(n,\gamma)^{165}Dy$; ^{113}In reacts with thermal neutrons as $^{113}In(n,\gamma)^{114m}In$, ^{115}In reacts with the 2.45 MeV neutron (fast neutron) as $^{115}In(n,n')^{115m}In$, and $^{115}In(n,\gamma)^{116m}In$[32]; ^{197}Au reacts with the 4.89 eV neutron as $^{197}Au(n,\gamma)^{198}Au$. Fig. 2–2 show each (n,γ) reaction cross section of ^{164}Dy, ^{115}In, and ^{197}Au. Dy, In, and Au are sensitive to specific energies. Dy reacts to thermal neutrons as $^{164}Dy(n,\gamma)^{165}Dy$. In reacts 2.94 x 10^4 b to the 1.46 eV neutron as $^{115}In(n,\gamma)^{116}In$. The Au reacts 2.73 x 10^4 b to the 4.89 eV neutron as $^{197}Au(n,\gamma)^{198}Au$. These reactions would be dominant and be employed to measure neutron fluxes through activation analyses.

Fig. 2–3 shows the configuration of irradiation experiments and simulations. The DD fusion device and samples were surrounded by polyethylene blocks and graphite blocks which moderate fast neutrons and enhance the reactions between material foils and wires and thermal neutrons. Material foils and wires were installed in the assembly to measure the spatial distribution of neutron by the activation analysis.

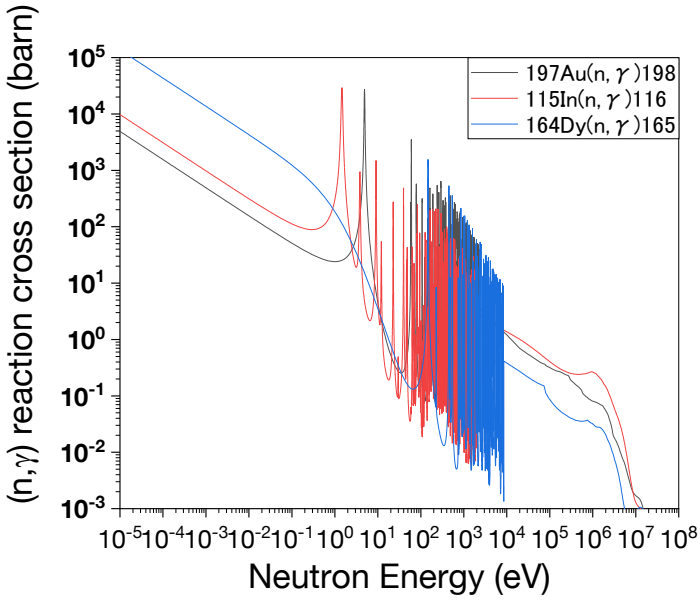

Fig. 2–2.a (n,γ) reaction cross sections of ^{197}Au, ^{115}In and ^{164}Dy by JENDL-4.0, drawn by log-log scale

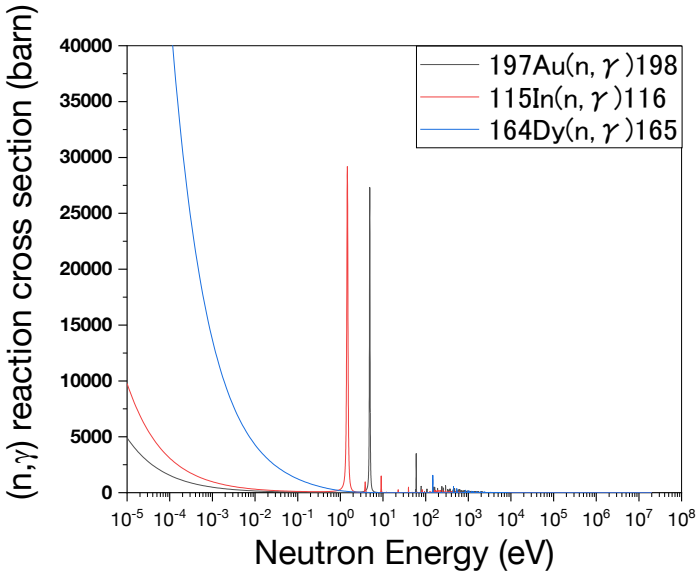

Fig. 2–2.b (n,γ) reaction cross sections of ^{197}Au, ^{115}In and ^{164}Dy by JENDL-4.0, drawn by linear-log scale

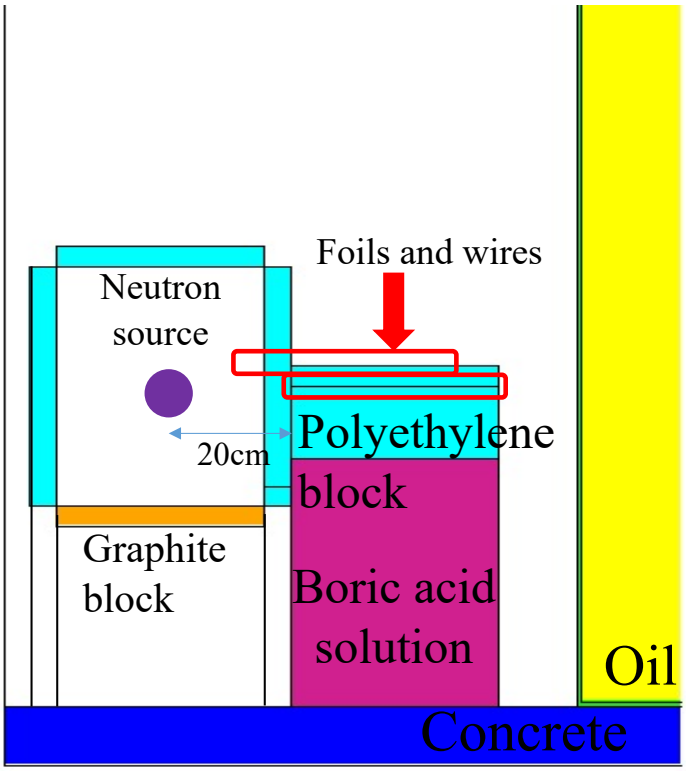

Fig. 2–3.a Cross-sectional view of the experiment and simulation of neutron transport:

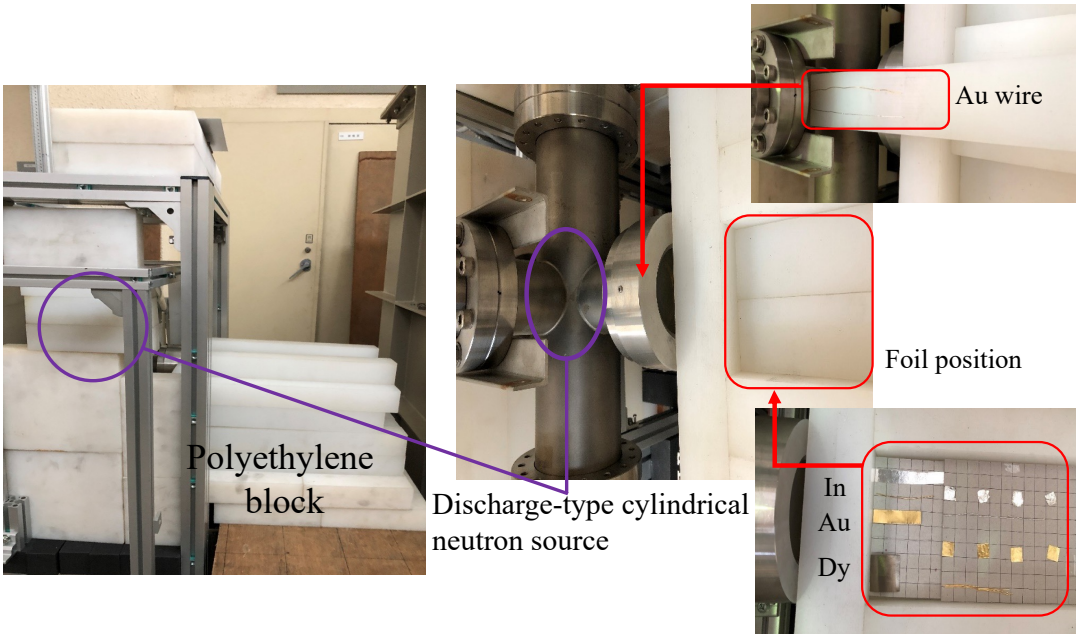

Fig. 2–3.b Experimental configuration: discharge-type cylindrical DD neutron source and polyethylene attenuating blocks where material foils were installed.

In this work, the simulation of neutron transport was performed by the Monte Carlo N-particle Code version 5 (MCNP5)[33]. ENDF/B-VII.1 and FENDL-3.0 nuclear libraries[34], [35] were employed for nuclear reactions. IRDFF-1.05 and JENDL-D99 dosimetry cross section libraries[36], [37] were employed for the (n,γ) reactions. The ENDF/B-VII.1 library was employed for Dy because there was no dosimetry data. The simulation was performed with the cylindrical volumetric source as large as the actual cathode. The neutron flux was calculated and converted into the total number of decays with the cross sections of the (n,γ) reactions. The total number of decays was given by following equations:

$$B = k \int_{t_1}^{t_2} A(t)dt \tag{2–1}$$

$$A(t) = \phi \, N_{total} \, \sigma_{(n,\gamma)} \left(1 - e^{-\lambda t_0}\right) e^{-\lambda t} \tag{2–2}$$

where,

$B(\mathrm{Bq \cdot sec.})$ is the total number of decays,

$A(\mathrm{Bq})$ is each activity of activation foils,

k is the constant dependent on the shape of an activation material

$\phi(/\mathrm{s}/\mathrm{cm}^2/\mathrm{sn})$ is the neutron flux per single neutron,

$N_{total}(\mathrm{neutrons})$ is the total neutron yield,

$\sigma_{(n,\gamma)}(\mathrm{cm}^2)$ is the (n,γ) reaction cross section of each nuclide,

λ is the decay constant of the created daughter nuclide,

$t_0(\mathrm{s})$ is the duration of irradiation,

$t_1(\mathrm{s})$ is the starting time of exposure to the IP,

t_2 (s) is the stopping time of a measurement.

Fig. 2–4 shows the geometry of the exposure from activation materials to the IP. The constant of k differs in shapes of activation materials. The read-out area of the IP was 1.0 mm x 1.0 mm, and the considered range of exposure was 126.87° of the cylindrical cross-sections for the wires. Foils were considered to emit half of the total radiations on the IP neglected to the thickness and self-absorption. Therefore, the constants of k were set to 0.3524 and 0.5, respectively. The neutron flux was simulated by MCNP5 and $\sigma_{(n,\gamma)}$ from the dosimetry cross section libraries. The equation (2–1) was considered to the half-life of the dominant nucleus individually.

Fig. 2–5 shows the decay scheme diagram of generated dominant radioactive isotopes and the emission rate of gamma-rays emitted from them simulated by DCHAIN-SP ver. 2014[38]. Both β-rays and γ-rays were emitted simultaneously during the exposure and were measured by the IP.

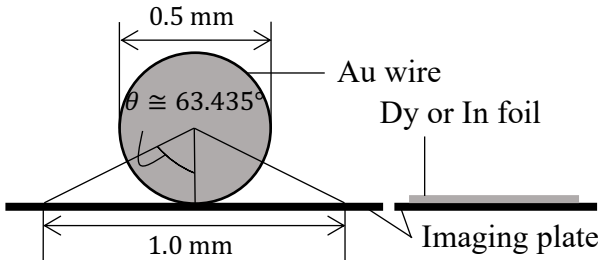

Fig. 2–4 Exposure from wire and foil to the IP considering the range of emission by angle and surface for each

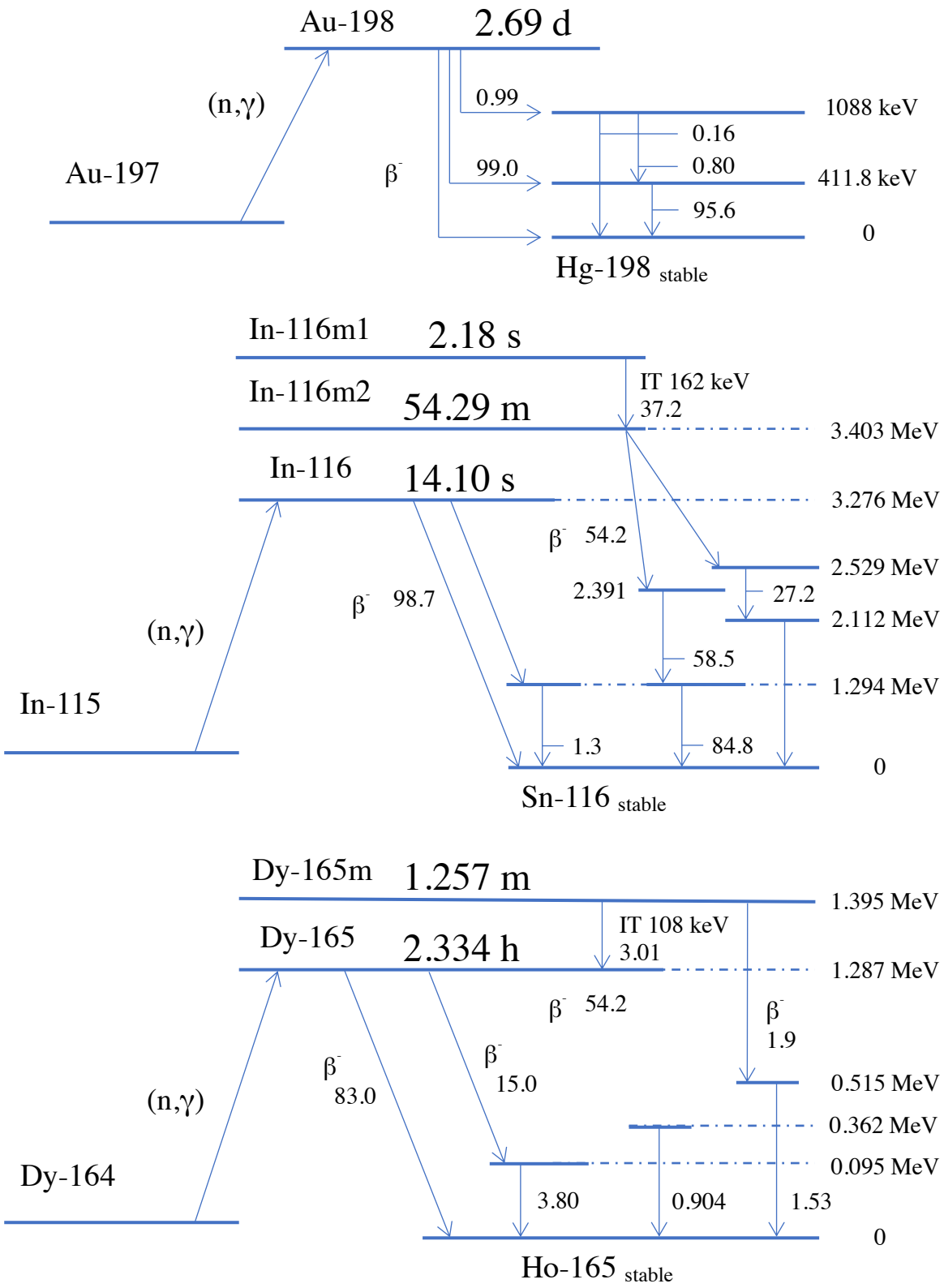

Fig. 2–5 Decay scheme diagrams of ^{197}Au, ^{115}In and ^{164}Dy

To calibrate the IP, a ^{137}Cs source which emits mainly 661.7 keV of γ-rays was employed. The activity of the ^{137}Cs source was 7.5 x 10^3 Bq in this work. The ^{137}Cs source was put on the IP for each required time. The calibration was performed in the darkroom to avoid fading the data[39] and both the ^{137}Cs source and the IP was covered with black cover. The room temperature was set to 20 °C during calibrations.

For the irradiation experiment and the activation analysis, foils and wires were irradiated by DD fusion device, and then materials were activated. After the irradiation, materials were put on the IP, and the IP was exposed to β-rays and γ-rays emitted from them. The data in the IP was read by a phosphor imager (Storm 820, Molecular Dynamics) which scanned the IP of 200 μm x 200 μm pixel resolution. After the read-out, the digital image was obtained which included the data of PSL. The net PSL (PSL/cm^2) was converted into the total number of decays (Bq x sec.) of β-rays and γ-rays. Finally, the total number of decays was employed for the comparison of the experimental and simulated results.

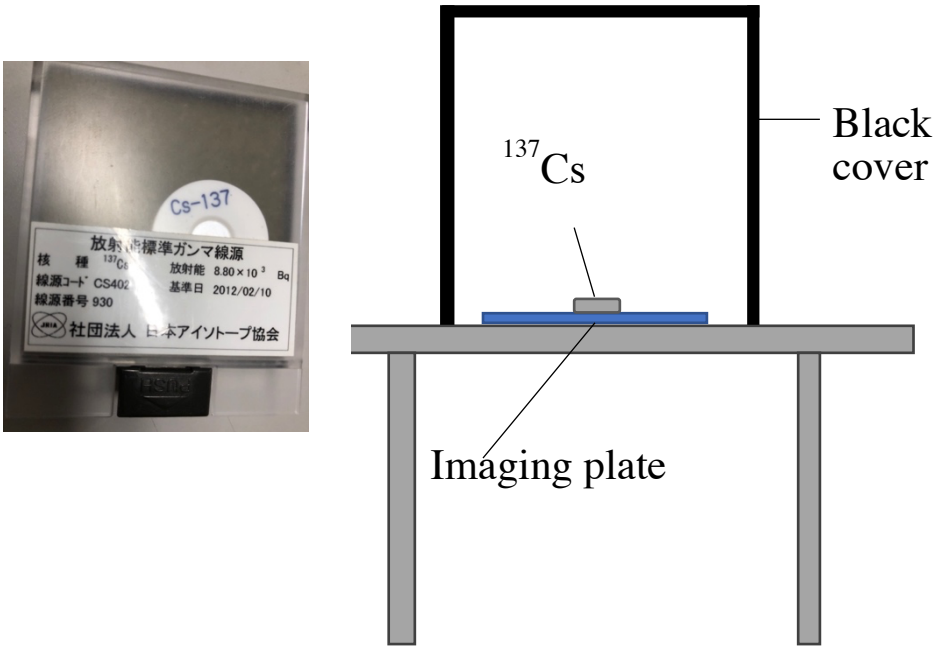

Fig. 2–6 The ^{137}Cs γ-ray source (left) and configuration of the IP calibration inside the dark room using the ^{137}Cs source (right)

Fig. 2–7 Fujifilm IP BAS-MS2025 (white), Molecular Dynamics Storm 820 Phosphor imager (upper right), GE Healthcare FLA Image Eraser (lower right)

2.3 Results and Discussion

2.3.1 Calibration of the IP with the ^{137}Cs source

Fig. 5. shows the calibration result of the IP with ^{137}Cs. The ^{137}Cs was put on the IP and irradiated it directly. ^{137}Cs was treated as the surface source whose radiation was almost half for one surface. The obtained relationship between net PSL (from 10^3 to 10^5 PSL/cm^2) and total number of decays defined as B (from 10^6 to 10^8 Bq·s) was almost linear as $B \propto P^{0.97}$. The slope of the relationship was similar to that of a NIP[40] because both the IP and the NIP were composed of the same PSL materials sensitive to radiations. The linearity between the net PSL induced by radiations and the total number of decays was confirmed for the dynamic range of 3 orders of magnitude.

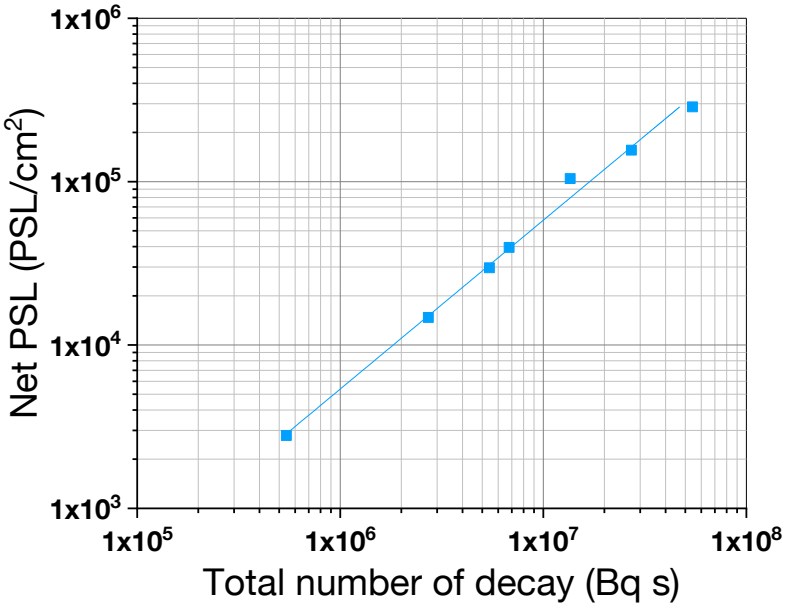

Fig. 2–8 The Relation of the net PSL obtained by the IP and the total number of decays of activation foils

2.3.2 NPR of DD fusion device

Fig. 2–9 shows the position of the installed ^{3}He counter. The neutron source emits X-rays by bremsstrahlung the surface of the between vacuum chamber and accelerated electrons, and the ^{3}He neutron counter is sensitive to X-rays. In the case of an neutron irradiation experiment using the non-covered ^{3}He counter, there were broad signals detected by lower channels shown in Fig. 2–10.a. In the case of an neutron irradiation experiment using the ^{3}He counter covered with lead sheet, there were less signals detected by lower channels shown in Fig. 2–10.b compared to Fig. 2–10.a. From these results, X-rays emitted from the neutron source were enough shielded to count neutrons by lead sheet.

Based on this result, the relation between results of neutron count by the ^{3}He counter was obtained, shown in Fig. 2–11. Neutron production rate obtained by the lead covered ^{3}He counter was 100 times lower than that of the non-covered ^{3}He counter due to the effect of X-ray signals. In this work, neutron production rate obtained by the lead covered one was employed and applied to activation analyses.

Fig. 2–9 Installed position of the ^{3}He neutron counter without lead sheet (left) and with lead sheet of 2 mm thickness rolled twice (right)

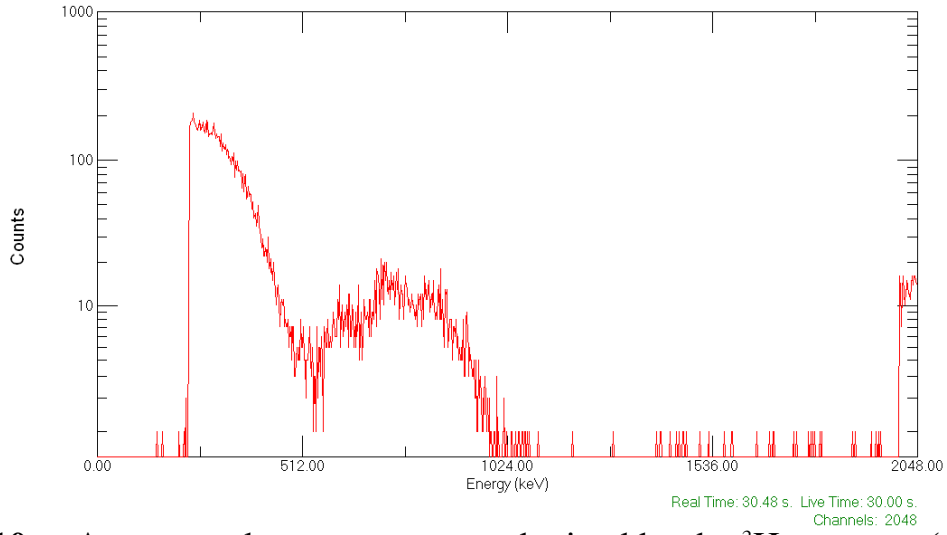

Fig. 2–10.a A measured count spectrum obtained by the ^{3}He counter (without lead)

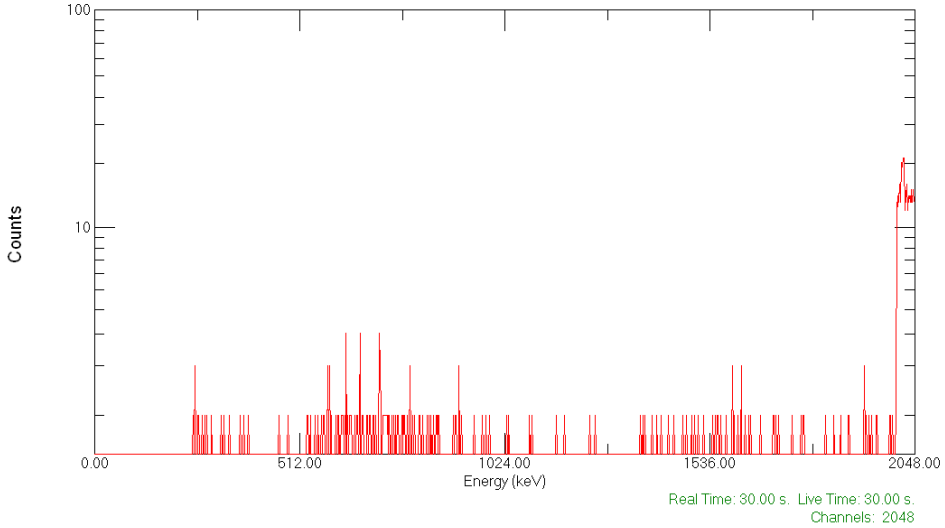

Fig. 2-10.b A measured count spectrum obtained by the ^{3}He counter (with lead)

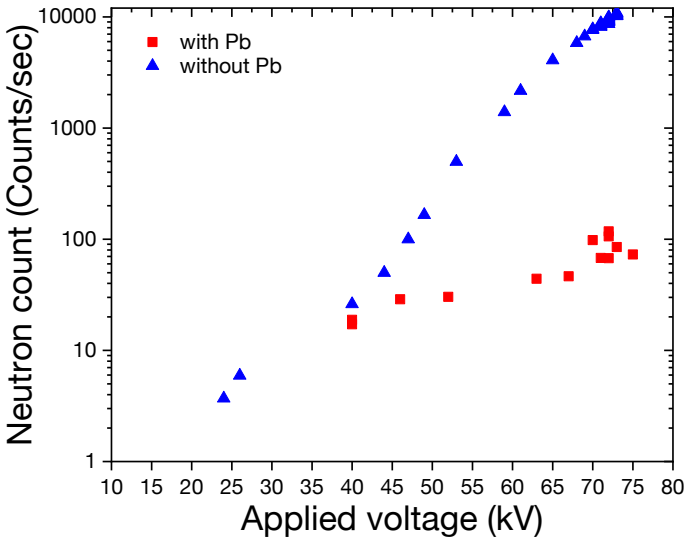

Fig. 2-11 The relation between results of neutron count by the ^{3}He counter

Fig. 2–12 shows the time transition of the NPR from the DD fusion device measured by the ^{3}He counter. To avoid the instability during an irradiation, the device's current and average voltage were controlled to 3.0 mA and 70 kV, respectively during the irradiation[41]. Since the glow plasma of the DD fusion device was stable during the irradiation, the obtained NPR was in the range from 1 x 10^5 to 2 x 10^5 n/s. The average NPR was 1.55 x 10^5 n/s. Sufficient neutron fluence in the model blanket assembly was obtained by this source within hours of irradiation.

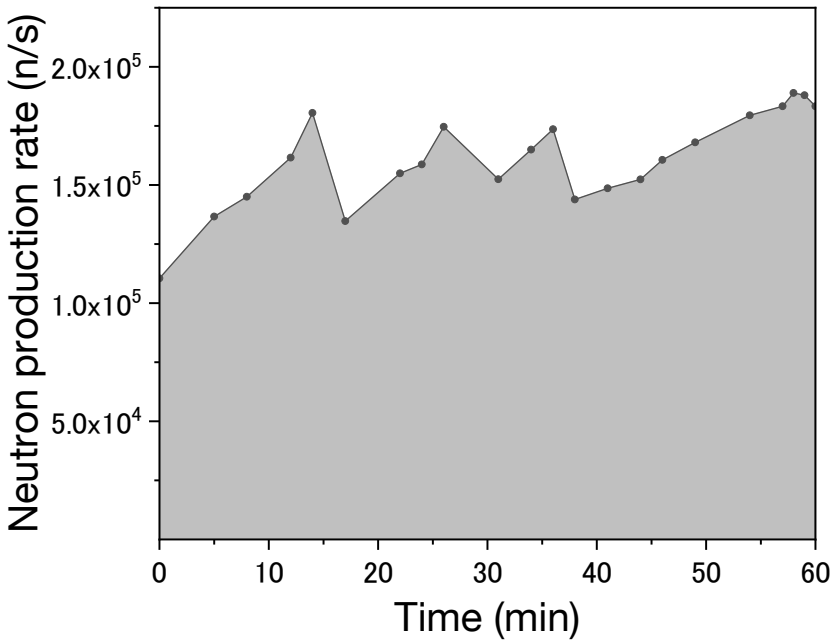

Fig. 2–12 One experimental result of NPR measured by the ^{3}He counter corrected by the X-ray effect

2.3.3 Comparison of computation and experiment

Fig. 2-13 shows the relative errors of simulated neutron fluxes at the centre of calculated positions set by each particle history (neutron per source, nps) from 1 x 10^5 to 5 x 10^7. On MCNP5, since it is generally reliable that the relative error is less than 0.1, the simulation case of nps = 5 x 10^7 was reliable enough to apply to the comparison with measured results. Fig. 2–14 shows the neutron fluxes divided into energy groups of below 0.1 eV, 0.1–100 eV, 0.1–100 keV, above 0.1 MeV, and total neutrons simulated by the particle history of 5 x 10^7. Neutron fluxes of low energy regions tend to be fluctuated for distant positions due to the shortness of reached particles. In this work, neutron fluxes between 5 and 32.5 cm were applied to the comparison with measurements, and the relative error of the total neutron flux was reasonable to the comparison.

Fig. 2–15 shows activation foils and wires after the irradiation and their digital images. The neutrons emitted from the fusion device came from

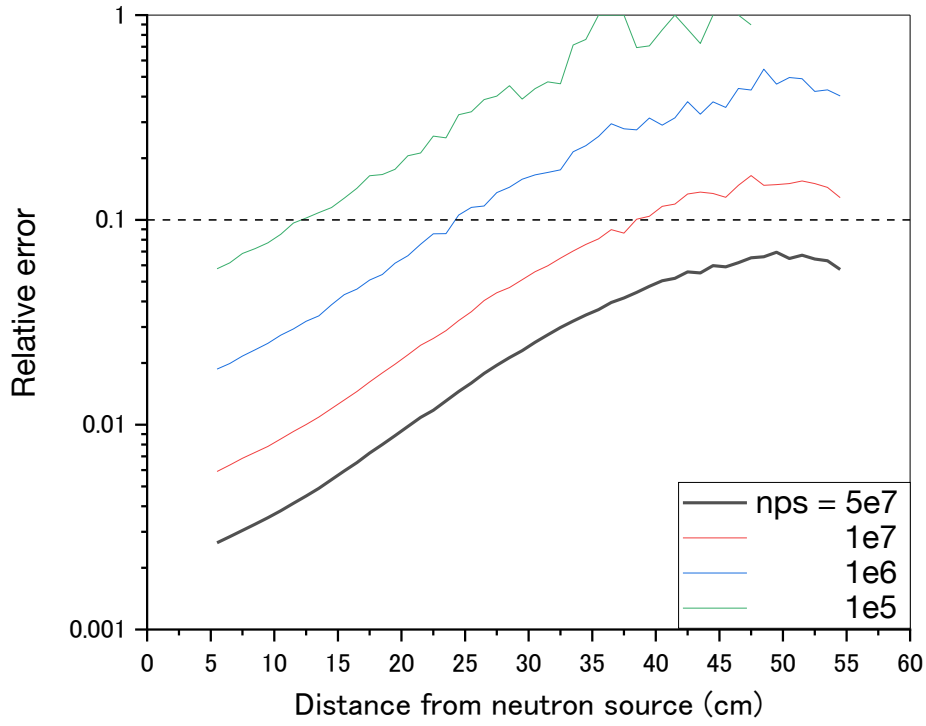

Fig. 2–13 The transitions of relative errors simulated by each condition of particle histories

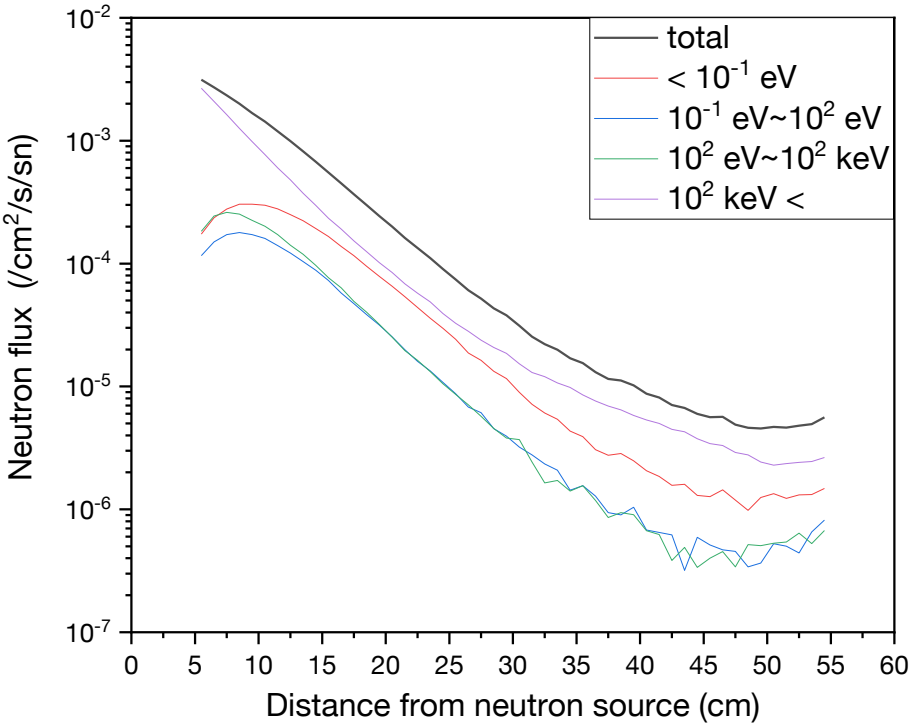

Fig. 2–14 The transitions of neutron fluxes divided into energy groups simulated by the particle history of 5 x 10^7

the upper side of images. These images show that the obtained PSL was reduced from upper side to lower side. The obtained PSL per area was converted into the total number of decays with the calibration result. The relation between the total number of decays and the distance from the DD fusion neutron source was shown in Fig. 2–16. The measured PSL converted to the total number of decays as a function of the position was then compared with the numerical analysis with MCNP5, shown in Fig. 2–16. Measured results were obtained by the interval of 0.5 cm (5 pixels in one area) and plotted in the figure.

As seen in the figure, plotted points were obtained by the measurement by the IP, bold lines indicate the calculated results considering the γ-rays, and each coloured region indicates the calculated results include the counts of β-rays. Since the calibration of β-rays was not performed in this work, the regions were considered the sensitivity of β-rays to IP. The experimental results of the Au wire and the Dy foil agreed with the simulated one in the single digit. The difference in the distant position about Au was caused by the small amount of the NPR. The experimental results of In foils were

largely underestimated from the computed results. The Dy foil has many natural isotopes (i.e., 18.91% of ^{161}Dy, 25.51% of ^{162}Dy, 24.90% of ^{163}Dy, 28.18% of ^{164}Dy, and others) and it arose the discrepancy. The In foils have two natural isotopes of ^{113}In and ^{115}In, and their reactions to neutrons vary compared with the results of Au. Generated radioactive isotopes of ^{114m}In and ^{116m}In have different production amounts and half-lives individually. These factors made the noticeable differences. In addition, β-rays and γ-rays emitted from radioactive isotopes vary by their decay processes. Sensitivities of the IP differ by energies of β-rays and γ-rays[42], [43]. In this work, the calibration of the IP was performed by ^{137}Cs which takes only 661.7 keV of γ-ray into account; therefore, the practical distribution of calculation results might have been in the regions of calculation results because the sensitivity of β-rays is different from γ-rays.

These results suggest that neutron fluxes measured with different activation materials reflect the different activation cross sections corresponding to the neutron energy region. However, to evaluate and benchmark the numerical calculation that provides detailed energy spectrum, further improvement of the activation analysis would be required.

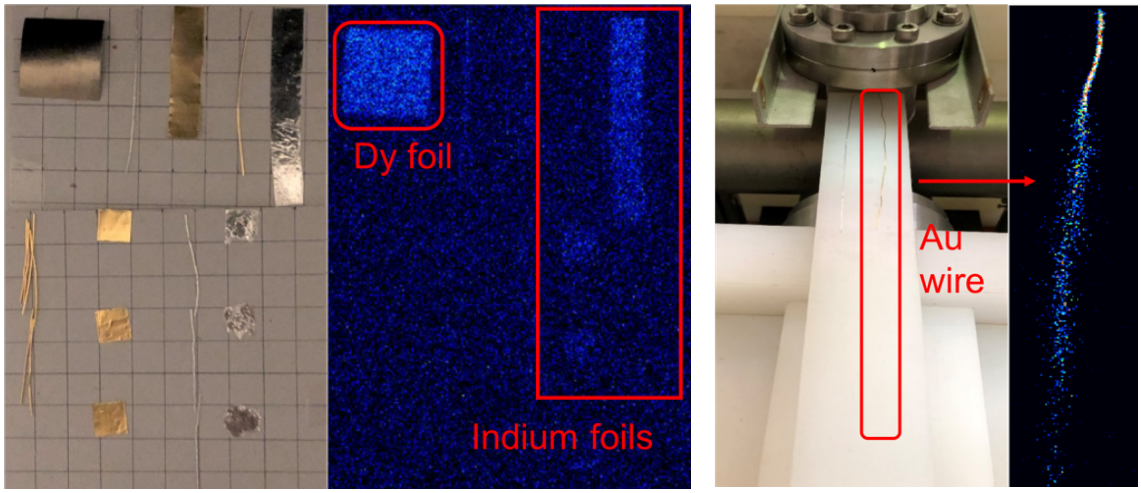

Fig. 2–15 Read-out results of Au, In, and Dy foils (left) and Au wire installed on the polyethylene block (right)

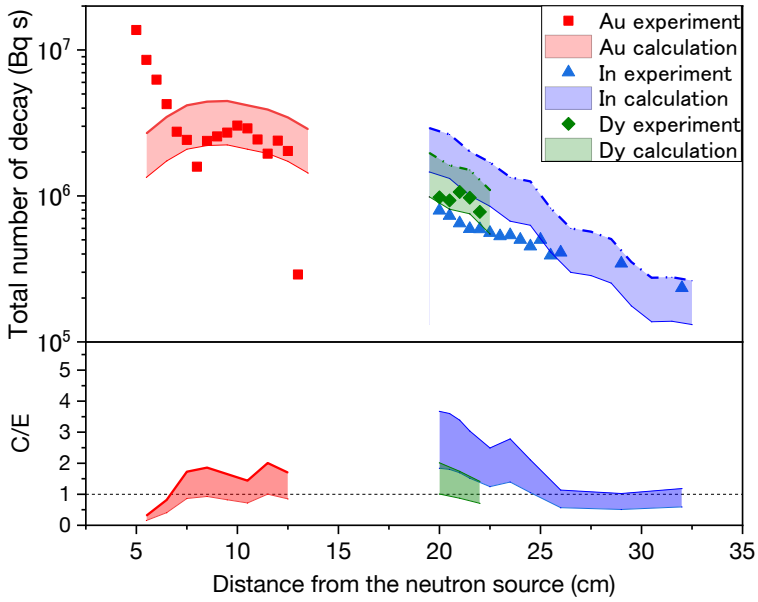

Fig. 2–16 Relations of calculations and experiments by total number of decays and calculation to experimental value (C/E) corresponding to the distance

2.4 Conclusion of Chapter 2

In this chapter, the measurement of the spatial distribution of the neutron with the IP and activation materials was proposed. The experimental results indicate that the IP had the linear relation between the value of PSL and the total number of decays, and it was applied to convert the PSL by the activation materials into the total number of decays.

The comparison between experimental and simulated results of the neutron fluxes were obtained, suggesting that a measurement of 2D and 3D neutron distributions using this method is enough feasible to be applied. Especially, based on the results of measured plots and simulated results, this method is possibly feasible to measure neutron fluxes by interval of 0.5 cm in this work.

Although the analytic results employing gold and dysprosium generally agreed with calculation at distant positions, the results measured with indium was largely underestimated compared to the calculation. It was mainly caused by their diversities of radioactive isotopes generated from the (n,γ) reactions by irradiated neutrons. For reducing the discrepancy between the experimental and simulated results, varieties of β-rays and γ-rays emitted from radioactive isotopes requires the detailed sensitivity correction by their kinds and energies. Considering these factors, the error analysis of calculation to experimental results would be performed in Chapter 3.

3. Measurements of neutron spatial distribution divided into specific energy regions inside a blanket mock-up

3.1 Introduction

Measurements of neutron spatial distribution and spectrum inside fusion blanket modules have been required for the self-sufficient evaluation of tritium breeding ratio (TBR). TBR is not uniform inside the blanket due to absorption by lithium (almost by the (n,t) reaction of lithium-6) and the neutron multiplying effect by beryllium or lead which depends on the design of breeding and multiplying layers and coolant types.

Neutronics experiments using a blanket mock-up have been reported for the benchmark of measuring neutrons by a neutron activation method[44]. Mock-up experiments were also performed for detecting and measuring tritium production using a liquid scintillation counter[18], [45], and tritium production performance was different by the depth of a breeding layer and neutron energy regions[17]. From these reports, measurements of thermal and epi-thermal neutron fluxes are required to evaluate tritium production inside the breeding layer. Material foils are planned to be transferred at the fixed positions inside the blanket module and be measured with a radiation dosimeter after irradiation of neutrons, called neutron activation system (NAS), to measure neutron fluxes. A foil-based activation system is planned to measure the neutron energy spectrum inside the blanket module[46], [47]. Since tritium production is widely distributed inside the breeding layer of the blanket module, it is essential to measure neutron spatial distribution of thermal, epi-thermal, and fast neutrons. Although the method of measuring spatial distribution of tritium production is required for the self-sufficiency of fusion reactors, it has not been confirmed yet.

This study aims to propose the method of measuring thermal and epi-thermal neutron fluxes inside a blanket mock-up. Experiments of neutron irradiation were performed, and an imaging plate and material foils were employed for an activation analysis. Material foils were simulated to be activated by irradiated neutrons for each targeted energy region of neutrons. Experimental results were compared with the simulation of neutron transport for the activation analysis, and the detection range of the IP was examined.

3.2 Methods

As shown in Fig. 3–1 and Fig. 3–2, irradiation mock-ups composed of graphite blocks (1.63 g/cm^3 of averaged density per unit, which was about 74% of theoretical density of graphite) were installed under and neighbouring a neutron irradiation source. These mock-ups were piled by graphite blocks or polyethylene blocks each of which was mainly 5 cm x 5 cm x 20 cm. One mock-up under the neutron source (a lower mock-up) was 10 cm x 20 cm x 40 cm, and another mock-up (an upper mock-up) was 25 cm x 20 cm x 30 cm.

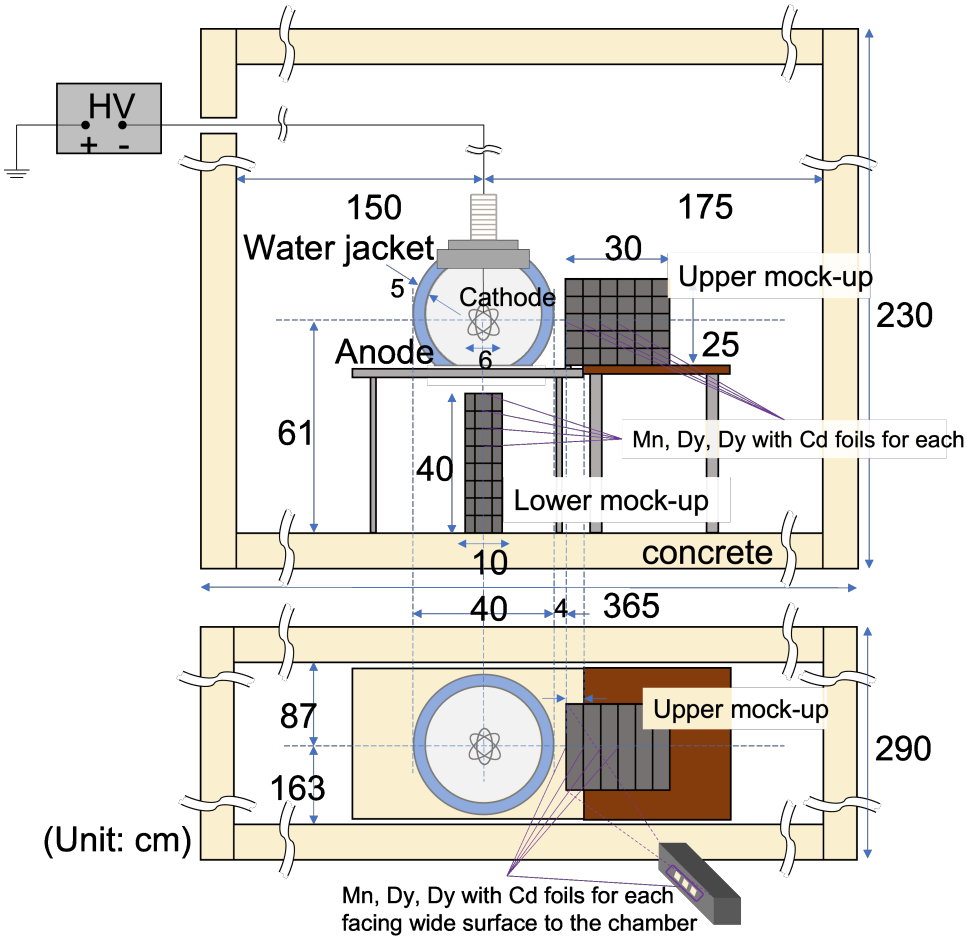

Fig. 3–1 The geometry of mock-up experiments and simulations: experimental devices and mock-ups were installed on the basement whose wall was set to 20 cm of concrete for simulations

Fig. 3–2 Configuration of mock-up experiments: mock-ups composed of polyethylene blocks (upper) and graphite blocks (middle), and material foils attached to each mock-up block (lower)

Material foils were installed inside both mock-ups. Referred by some reports about the activation foil method, dysprosium (Dy) (0.25 mm thickness) and manganese (Mn) (1.00±0.05 mm thickness) were employed in this study. In addition to this, Dy sandwiched by cadmium (Cd, 0.5 mm thickness) was employed. Each target of neutron energy region was below 1 eV (thermal) for Dy, between 1 eV and 1 MeV (epi-thermal) for Dy with Cd, and thermal and epi-thermal for Mn, respectively. Material foils of Dy and Mn were cut into pieces of about 1 cm x 1 cm. Each piece of Dy, Dy with Cd and Mn was attached to one block 1 cm distant together. Wide surface (the surface of 1 cm x 1 cm) of each foil was faced to the neutron source, and positions of installations were shown in Figure 3–3. Each distance between foil positions were set to 5 cm.

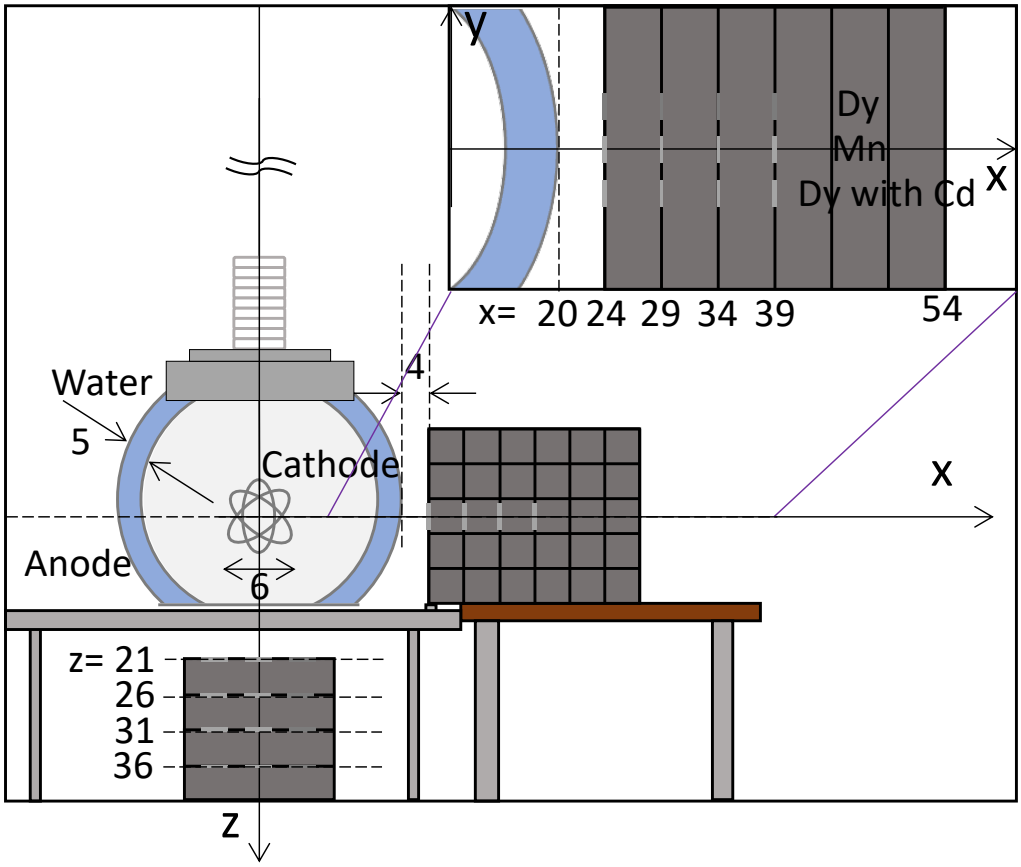

Fig. 3–3 Foil positions installed inside lower and upper mock-ups, respectively

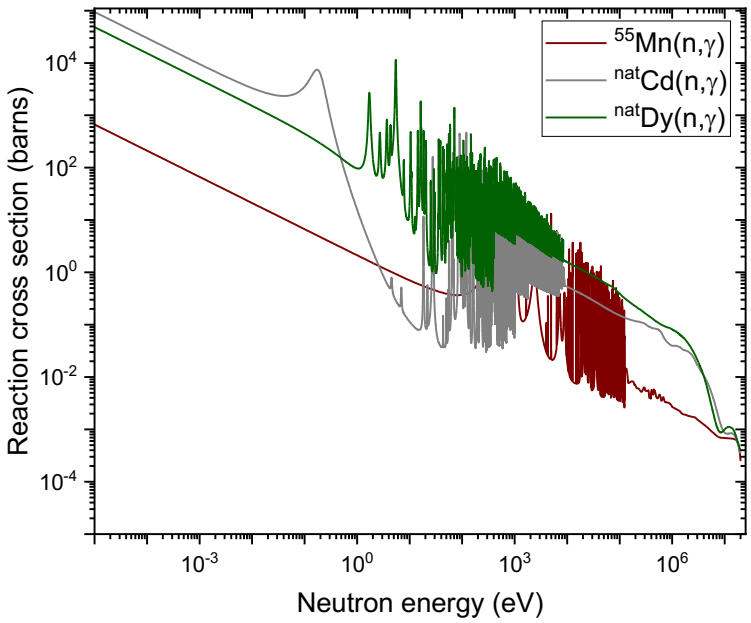

Fig. 3–3 (n,γ) reaction cross section of material foils by JENDL-4.0 [71]

Neutron irradiation was performed by the discharge-type deuterium-deuterium fusion neutron source[48], [49]. The cathode inside a vacuum chamber was spherical and basket shape with the diameter of 5 cm and was made of molybdenum. The shape of the vacuum chamber was also spherical and was made of stainless steel with the inner diameter of 15 cm and the outer diameter of 20 cm. The vacuum chamber excluding its bottom was covered by a water jacket circulated between the inner and outer surfaces which was kept at 10 °C (283 K) for the coolant of chamber components. Outer surface of the chamber was set to ground, which functionates as anode. Irradiated neutrons of monochromatic 2.45 MeV were generated by the deuterium-deuterium fusion reaction via glow discharge. For the stable operation of the neutron source with neutron production rate (NPR) of more than 10^7 n/sec., applied voltage, current and pressure inside the main chamber were kept between 60–65 keV, 30–40 mA (PS/PK125N060, Glassman high voltage inc.) and 1.56–1.64 Pa, respectively.

NPR during irradiation was measured by a cylindrical ^{3}He gas-filled counter covered by polyethylene and lead sheet (2 mm thickness). Removing the effect of incidents from other radiations or unknown factors, neutrons were counted by designated channels of 2000–5500 (comparison with the

whole channel of 0–8191) to avoid low and high channel noise. For the calibration of the ^{3}He counter, a ^{252}Cf spontaneous fission source (663 n/sec.) was installed inside the centre of the vacuum chamber. During the calibration, the ^{252}Cf source was kept inside the chamber for 94.5 hours and the cumulative values obtained between channels of 2000–5500 were employed.

For the activation analysis, an imaging plate (BAS-MS2025, Fujifilm) of two-dimensional dosimeter was employed. The IP has sensitivity to α-rays, β-rays, and γ-rays and there are different sensitivities among them. After the neutron irradiation to the foils, foils were kept for 30 minutes for avoiding the effect of γ-rays emitted by short half-life radionuclides (this process hereinafter called cooling time). After cooling time, activation foils were put on the IP and the exposure was performed. Experiments of exposure were, same as the activation experiment, performed with the black cover in the dark room whose temperature was kept at 20 °C. The exposure time was set for 20 hours because of the ratio of generated radionuclides. Dominant radionuclides were ^{56}Mn from the ^{55}Mn(n,γ) reaction and ^{165}Dy from the ^{164}Dy(n,γ) reaction during the exposure time. After exposure, the IP was kept for 100 hours in this study for avoiding the effect of fading. After fading, the read-out data was obtained by a phosphor imager (Storm 820, Molecular Dynamics).

The IP was calibrated employing a ^{137}Cs γ-ray radiation source and a ^{90}Sr β-ray radiation source, shown in Fig. 3–4. The ^{137}Cs source (7048.4 Bq at the beginning of the first calibration) mainly emits γ-rays of 662 keV and the ^{90}Sr source (9785.3 Bq at the beginning of the first calibration) mainly emits β-rays with maximum energies of 546 keV. One side of the ^{137}Cs source is covered by an acryl layer (3 mm thickness) which shields β-rays with maximum energies of 514 keV and 1176 keV, and another side has a small window which is covered by an aluminium film (0.1 mm thickness). It

Fig. 3–4 Standardised β- and γ-ray radiation sources with radionuclides of ^{90}Sr and ^{137}Cs

was reported that sensitivities of the IP to β- and γ-ray were different, and the sensitivity of β-ray was greater than that of γ-ray in the case of employing a ^{137}Cs source. In this study, therefore, the covered side was faced to the IP for avoiding the effect of β-rays. Both sides of the ^{90}Sr source are covered by polyester films with aluminium vapor deposition (less than 1 mg/cm^2). A fading effect of the IP was measured employing the ^{137}Cs source. The duration of exposure of gamma-rays was set to 10 min. and fading time was set from 1 min. (whose condition was read the IP immediately after exposure) to 7600 min. Experiments were, same as the activation experiment, performed with the black cover in the dark room whose temperature was kept at 20 °C.

From the activation analysis, the experimental result was obtained converted from PSL value into the total number of radiations emitted from activation foils by a following equation:

$$A = \frac{a_\beta \times p^{b_\beta} + a_\gamma \times p^{b_\gamma}}{P} \times e \times r \qquad (3\text{–}1)$$

were,

A: total number of radiations (Bq · sec./source)

a_β, a_γ and b_β, b_γ: calibration factors obtained by each radiation of β- and γ-ray

p: averaged PSL value (PSL/pixel)

P: total neutron production obtained by the ^{3}He detector (neutrons)

e: sensitivity of radiations standardized by the ^{137}Cs source and the ^{90}Sr source for each radiation

r: emission rate of each activation foil per decay process

Table 3–1 shows each half-life, radiation type, emission rate, and sensitivity standardized by the calibration sources and emission rate of principal radiations emitted from the calibration sources and activation foils. ^{137}Cs was employed for the γ-ray source which emits each β-ray of 514 keV and 1176 keV, and γ-ray of 662 keV. As described above, the ^{137}Cs source was covered with the acrylic container and it shields β-rays during exposure to the IP. ^{90}Sr was employed for the β-ray source which emits β-ray of 546 keV. The ^{90}Sr source reaches the equilibrium between production and decay of Y-90 soon, and the effect from radiations emitted from the decay of Y-90 is insignificant in this work. ^{56}Mn was employed for the activation materials which emits each β-ray of 2.849, 1.038 and 0.736 MeV and each γ-ray of 0.847, 1.811 and 2.113 MeV. ^{165}Dy was also employed for the activation materials which emits each β-ray of 1287, 1192 and 292 keV and γ-ray of 94.7 and 362 keV. Each sensitivity was obtained by G. Boutoux *et al*.[50], Y. K. Haga *et al*.[42], A. Taniyama *et al*.[43], and H. Ohuchi *et al*.[51] based on the emission rate, and each value were standardised by ^{137}Cs for γ-ray and ^{90}Sr for β-ray. In this work, those values of emission rate and sensitivity, shown in Table 3–1, were employed for the calculation of Eq. (3–1).

Numerical simulations of neutron transport and activation analysis were performed by PHITS[52] and DCHAIN-SP[38], [53] which is the included package of PHITS. The simulated geometry was shown in Fig. 3–1 excluding the supporting frame made of aluminium, a plate made of wood (brown colour), and an insulator. The thickness of walls of the irradiation room was defined as 20 cm for each, and outer side of walls were set to the calculation boundary.

After the simulation of neutron transport, a simulation of the activation analysis was performed by DCHAIN-SP with the neutron activation cross section data library FENDL/A-2.0[54]. The duration of neutron irradiation was set for 3 hours. Each activity of radionuclides generated by nuclear reactions were calculated.

For the consideration of uncertainties, each error was considered as below: 10% of measurement error for the IP; 2% of measurement error for the ^{3}He counter; calibration errors calculated by non-linear fittings; relative errors calculated by PHITS/DCHAIN-SP which includes errors of neutron transport occurred by the number of particle histories, geometric uncertainty, and nuclear data.

Table 3–1 Characteristics of radioactive nuclides

Nuclide	half-life	Radiation type	Energy		Emission rate		Sensitivity	
		beta/gamma	MeV	keV	% gamma-ray rate to Cs-137	beta-ray rate to Sr-90	gamma-ray	beta-ray
Cs-137	30.1671 y	beta	0.514	514	94.4	0.9440		0.9854
		beta	1.176	1176	5.6	0.0560		0.0280
		gamma	0.662	662	85.1	0.8510	0.8510	
Sr-90	28.79 y	beta	0.546	546	100.0	1		1
(Y-90	64 h	beta	2.28	2280	100.0)			
Mn-56	2.5789 h	beta	2.849	2849	56.3	0.5630		0.2179
		beta	1.038	1038	27.9	0.2790		0.1701
		beta	0.736	736	14.6	0.1460		0.1175
		gamma	0.847	847	98.9	0.9890	0.9341	
		gamma	1.811	1811	27.2	0.2720	0.2116	
		gamma	2.113	2113	14.3	0.1430	0.0953	
Dy-165	2.334 h	beta	1.287	1287	82.7	0.8270		0.3933
		beta	1.192	1192	15.0	0.1500		0.0750
		beta	0.292	292	1.7	0.0170		0.0278
		gamma	0.0947	94.7	3.6	0.0360	0.7200	
		gamma	0.362	362	0.8	0.0084	0.0093	

3.3 Results

3.3.1 Calibration of fading effect and sensitivities to β- and γ-ray of the IP

Fig. 3–4 shows the relation of read-out value to fading time. Though the fading effect was reported, it was not suited in this condition of this work. The averaged PSL steeply decreased until 1000 min., and became moderate after about 2500 min. Since the averaged PSL after 5 days was about 0.8 as low as the initial (1 min. after exposure) value, fading time was set to 100 h in this work. Compared with the reported results[39], the fading effect measured in this work was not significant.

Fig. 3–5 shows calibration results of the IP. The calibrated region obtained by β-rays was between 500–70000 PSL/pixel (about 100000 PSL is the limit) due to the intensity of the ^{90}Sr source, and the calibrated region obtained by γ-rays was between 2–300 PSL/pixel. Non-linear fitted carves were drawn on the same figure and the equations with standard errors were shown inside the legend. The fitted errors were caused by each measurement error of plotted values and fading effects.

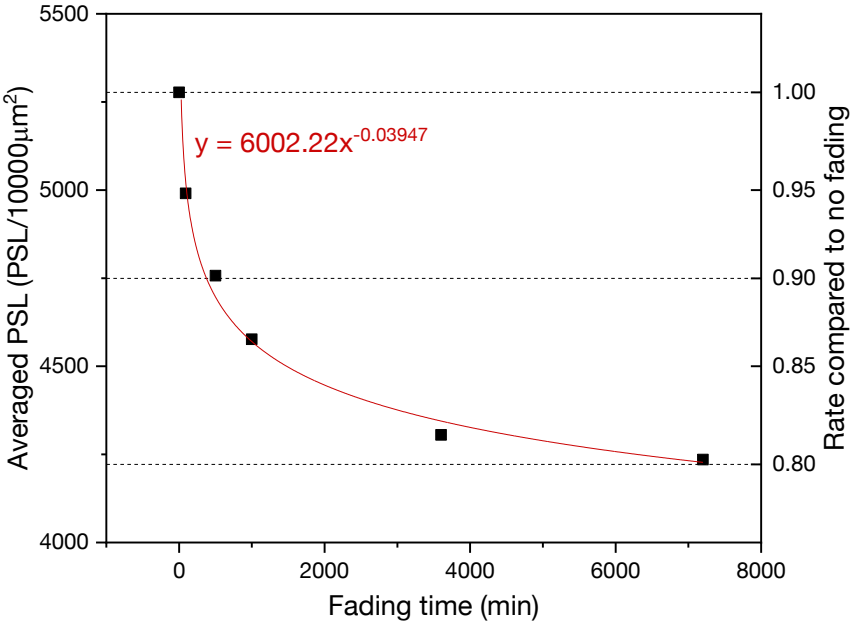

Fig. 3–5 The relation between averaged PSL and fading time

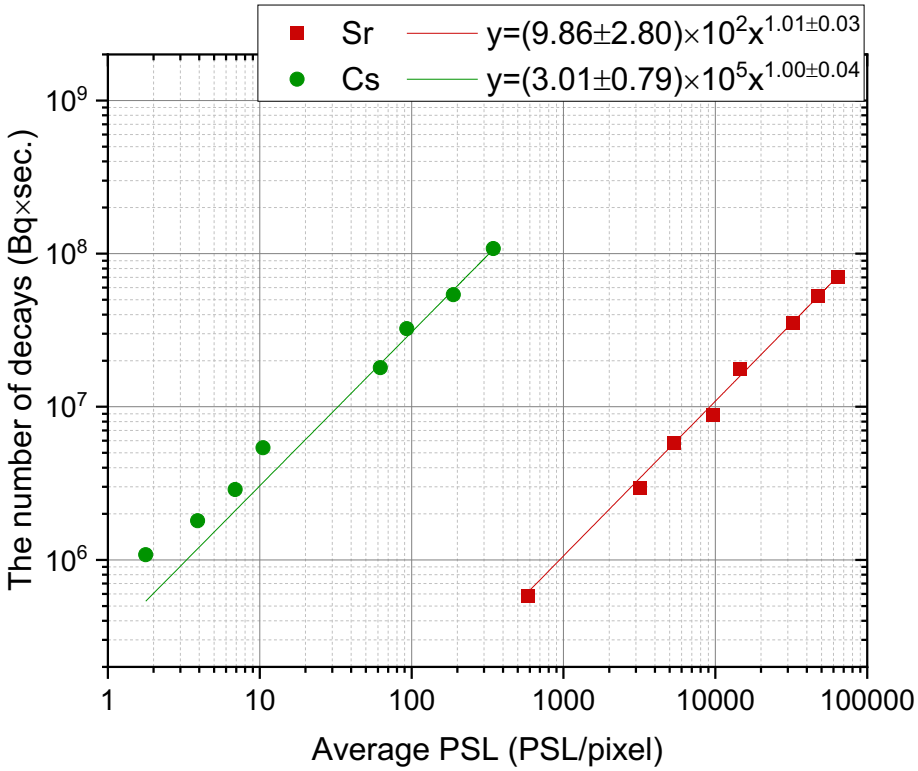

Fig. 3–6 Calibration results of the IP to β- and γ-rays employing the ^{90}Sr source and the ^{137}Cs source, respectively

3.3.2 Neutron fluxes at the position of material foils

Fig. 3–7 and Fig. 3–8 show neutron fluxes at each foil position with several distances from the vacuum chamber of L = 21 cm (lower mock-up) and 24 cm (upper mock-up). Peak fluxes of fast neutrons by lower mock-ups were higher than that by upper mock-ups because of the water jacket of vacuum chamber. The neutron fluxes of Dy and Mn showed almost similar trends. In the case of graphite mock-ups, there were significant differences between lower and upper mock-ups in the range of thermal, below 0.03 eV, region. Compared to the upper mock-up, thermal neutron fluxes were higher at the Mn position and were low at the Dy position for the lower mock-up. Those differences were caused by the positions and distances from the centre of the vacuum chamber. Since there was the water jacket between the upper mock-up and the vacuum chamber, neutrons were attenuated and

Fig. 3–9 and Fig. 3–10 also show neutron fluxes at each foil position with several distances from the vacuum chamber. In the case of polyethylene mock-ups, the thermal regions of Dy and Mn were about twice as high as the result of graphite mock-ups because of the effect of attenuation. The neutron fluxes of Dy covered by Cd were different in the region of thermal neutrons due to the neutron capture reaction of Cd.

Compared with calculated results of Dy and Mn, neutron fluxes were almost same in fast and epi-thermal regions, and there were significant differences in thermal regions about every cases. This difference resulted in the comparison of each activity by neutron irradiation in the thermal region of neutrons. In the case of Dy with Cd, neutron fluxes in thermal regions were lower than results of Dy and Mn by more than 1 digit. This difference was caused by covering Cd which absorbed thermal neutrons.

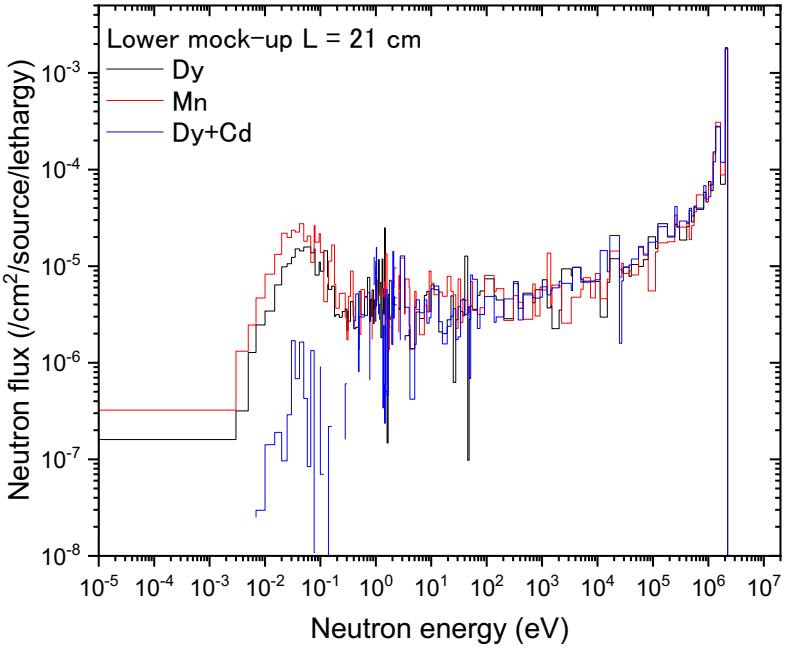

Fig. 3–7 Neutron fluxes at each position of material foils: L = 21 cm from the center of the vacuum chamber to lower mock-up of graphite

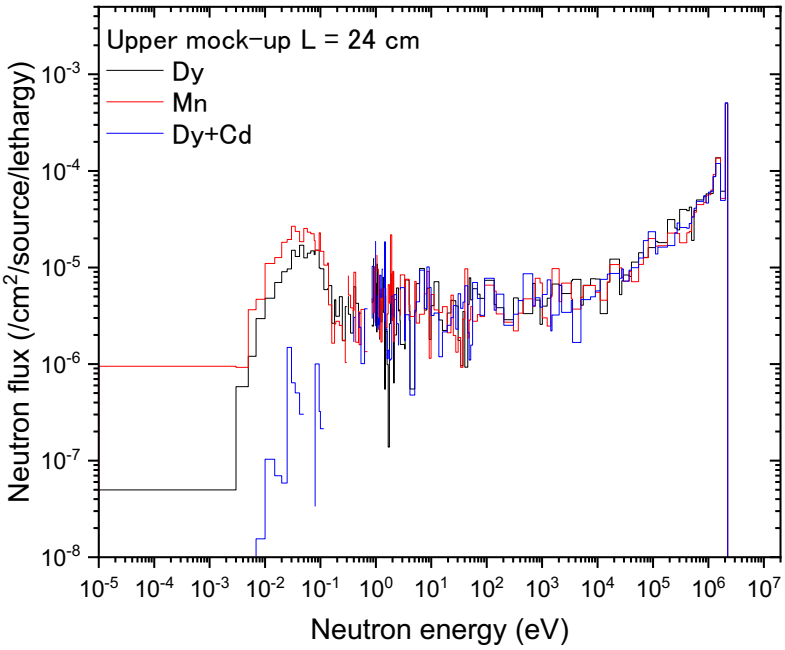

Fig. 3–8 Neutron fluxes at each position of material foils: L = 24 cm from the center of the vacuum chamber to upper mock-up of graphite

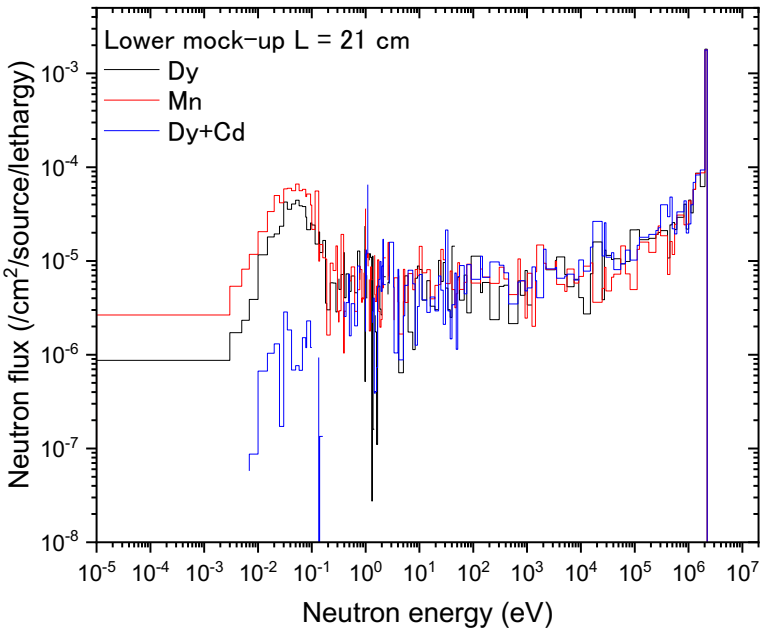

Fig. 3–9 Neutron fluxes at each position of material foils: L = 21 cm from the center of the vacuum chamber to lower mock-up of polyethylene

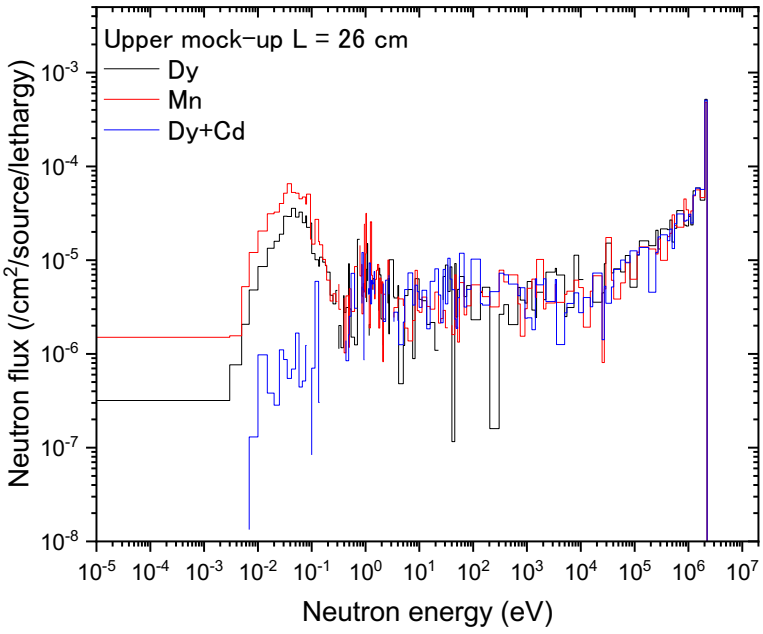

Fig. 3–10 Neutron fluxes at each position of material foils: L = 24 cm from the center of the vacuum chamber to upper mock-up of polyethylene

3.3.3 Cumulative ratio of (n,γ) reactions

Fig. 3–11 shows the simulated results of cumulative ratio of (n,γ) reactions divided into specific energy regions of fast, epi-thermal, and thermal neutrons with graphite mock-ups. Dy was mainly reacted with thermal neutrons installed at both lower and upper mock-ups. Results of Dy and Mn were reacted with thermal neutrons dominantly, and it was not changed significantly between the measured intervals. Results of Dy with Cd were reacted with epi-thermal neutrons, and each ratio was almost between 0.7–0.8 except for the most distant result of upper mock-up.

Fig. 3–12 shows also the simulated results of cumulative ratio of (n,γ) reactions with polyethylene mock-ups. Compared to the results of graphite mock-ups, each cumulative ratio of thermal regions was highly dominant for Dy and Mn. In contrast, results of Dy with Cd were reacted with thermal and epi-thermal neutrons and those ratios were changed by intervals.

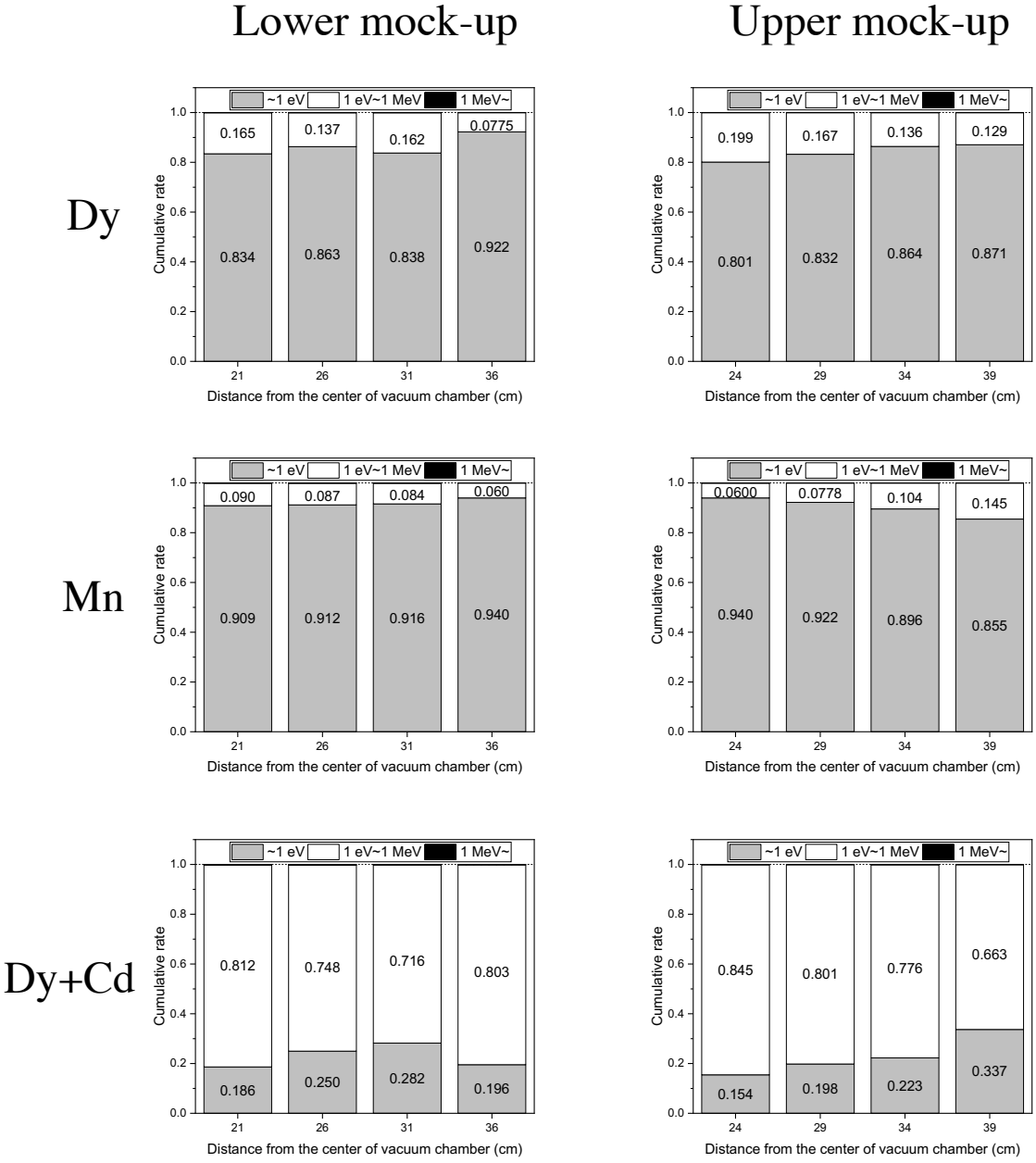

Fig. 3–11 Simulated results of accumulated rate of the number of (n,γ) reaction divided into thermal, epi-thermal and fast regions for each activation foils installed in the graphite blocks

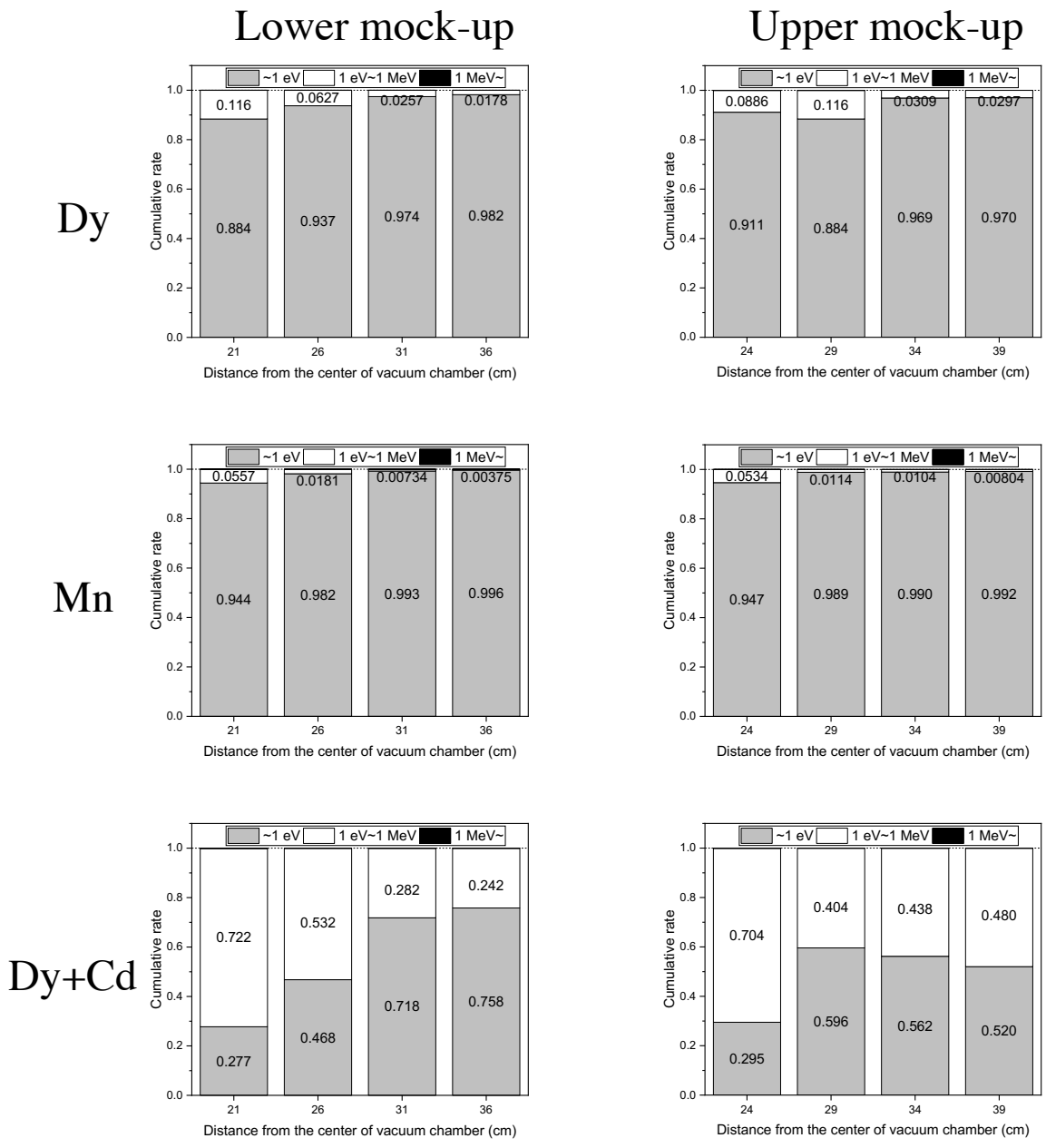

Fig. 3–12 Simulated results of accumulated rate of the number of (n,γ) reaction divided into thermal, epi-thermal and fast regions for each activation foils installed in the polyethylene blocks

3.3.4 Activation analyses and comparison with simulation results

Fig. 3–13 shows the experimental results of the activation analysis using the IP. The results of Dy and Mn were clearly obtained, and the results of Dy with Cd were less clear than them of Dy and Mn. This difference was caused by the amount of activity by neutron irradiation.

Fig. 3–14 shows the S/N ratio of experimental results with numbers corresponding to Fig. 3–14. S/N ratio was calculated by each variance of obtained value of PSL averaged by regions shown in Fig. 3–14 and obtained value of background PSL. The results close to the chamber side were almost agreed with signals from background noises. In contrast, the results distant from the chamber side were almost 1 to 3 of S/N ratio.

Fig. 3–15 shows the relations of neutron fluxes divided into energy regions, measured number of decays from each activation foil, and calculation to experimental value (C/E) to distance from the centre of vacuum chamber in the case of graphite mock-ups. Measured results decreased regarding the transition of neutron fluxes with distance. For about the C/E value, these results were 0.3 to 2.0, and error bar was calculated with experimental errors from devices, calibration errors and simulated errors. Most of these values were in the unity considering the error bar, and some points of Mn and Dy with Cd obtained at distant positions were not agreed even when each error bar was considered.

Fig. 3–15 also shows the relations of neutron fluxes, measured number of decays, and C/E to distance from the centre of vacuum chamber in the case of polyethylene mock-ups. Compared to the case of graphite mock-ups, thermal and epi-thermal neutron fluxes increased in the region of polyethylene mock-ups due to the moderation. For about the C/E value, these results were 0.5 to 2.5. Compared to the case of graphite mock-ups, the C/E values of Dy were slight disperse, and C/E values of Mn and Dy with Cd obtained at distant positions were slightly increased. This difference resulted from the amount of neutron fluxes inside the mock-ups.

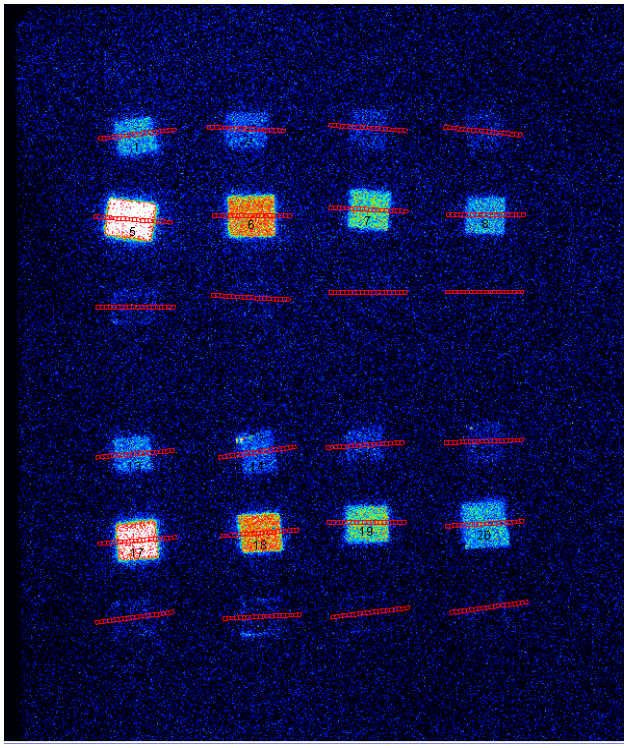

Fig. 3–13 Experimental results of the activation analysis using the IP and the measured regions divided into units by 1 x 1 mm^2 corresponding to **Fig. 3–14** (graphite mock-up, 3 h exposure)

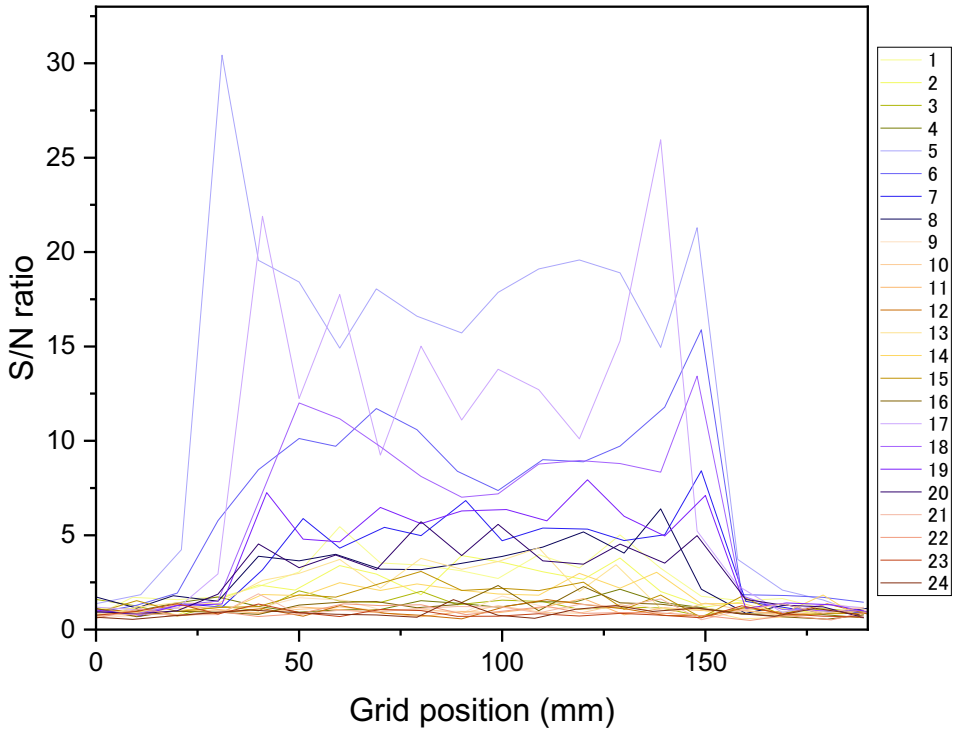

Fig. 3–14 Transitions of S/N ratio of experimental results

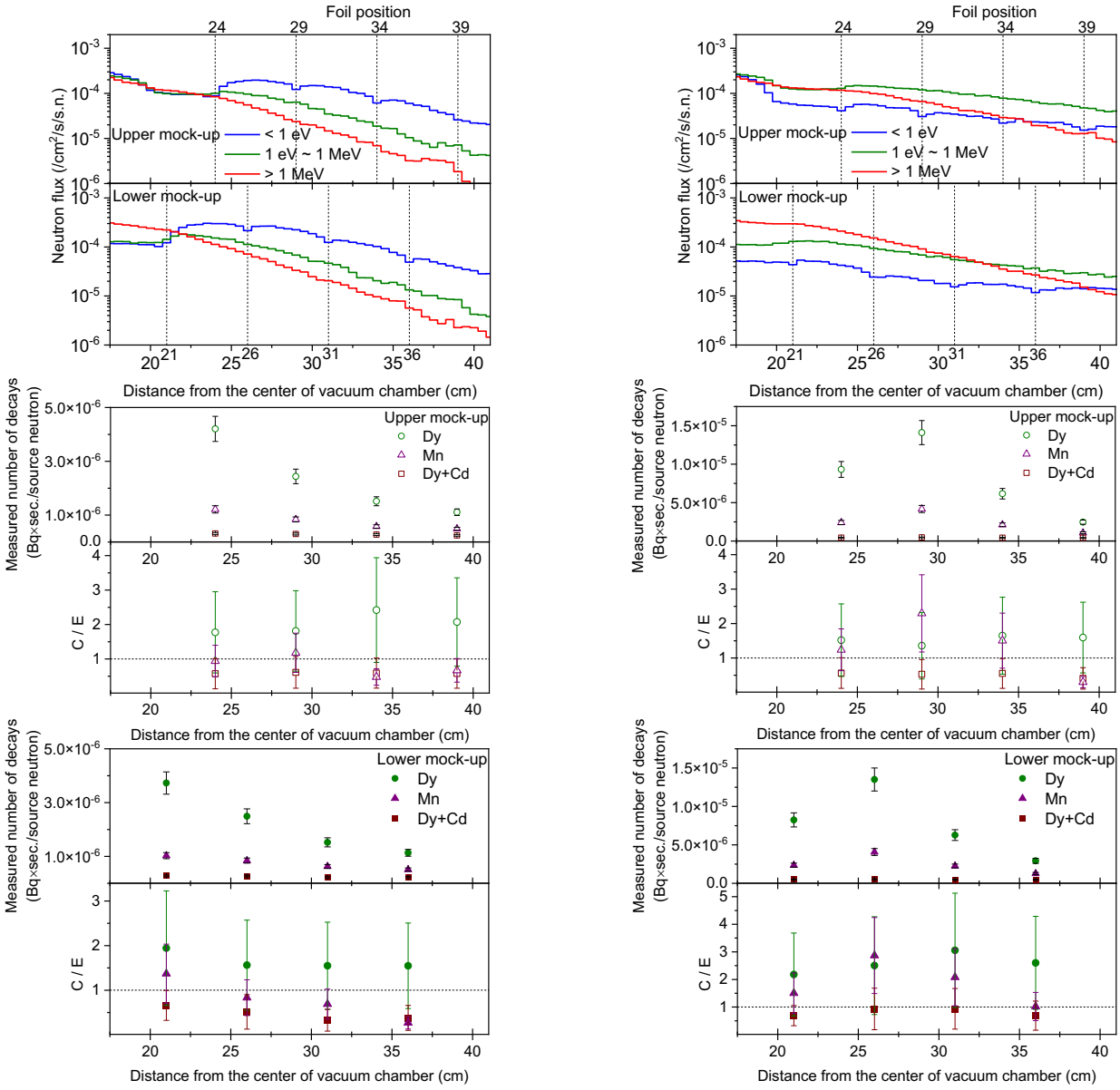

Fig. 3–15 Relations of neutron fluxes, measured number of decays and Calculation to Experimental value obtained by graphite mock-ups (left) and polyethylene mock-ups (right)

3.3 Conclusion of chapter 3

In this study, the neutron fluxes of thermal and epi-thermal regions were measured using the IP and the collaboration of material foils. Irradiation experiments to the mock-ups were performed with an average neutron production of 1.22 –1.31 x 10^7 n/sec., and the detection range of the IP at measured positions were between 2 x 10^{-3} and 5 x 10^{-2} cm^2/n calculated from the neutron fluences at foil positions in this work. Material foils were simulated to be activated by each targeted energy region inside the mock-ups, and the calculation to experimental values were 0.27–2.47. Discrepancies of calculated and experimental results were mainly caused by the calibration of the imaging plate, which affected the fading effect and measurement error of the imaging plate. The C/E values of Mn and Dy with Cd foils were significantly below 1, which was mainly caused by the shortness of neutron fluences in this system. Although this method of using the imaging plate and material foils requires for improving the accuracy of measurement, it could be possibly applied to evaluate tritium production.

The calibration error was slight significant compared with other error factors mostly due to the fading effect. For about the combination of material foils, Dy and Mn were reacted with thermal neutrons in every case and obtained C/E values were almost agreed. Dy with Cd was reacted with thermal and epi-thermal neutrons. For measuring thermal neutrons and epi-thermal neutrons dividedly, the thickness of Cd covering is required for considerations.

4. Simulations for practical measurement methods of spatial neutron distribution inside blanket mock-up irradiated with DT neutrons

4.1 Introduction

Blanket modules installed in a fusion reactor have been employed for neutron multiplication, heat transfer, tritium breeding, and bio shielding [55]. Tritium breeding is essential for the self-sufficiency of fusion fuel, and tritium breeding ratio (TBR) is required for more than unity or 1.05 with uncertainties of the evaluation, permeation, and other factors on fuel cycle [56]. Neutronics simulations have been carried out for the design of ITER test blanket modules (TBM) and DEMO blanket modules, the required performances have been determined[57], [58]. Experimental evaluations have also been reported with a blanket mock-up performed for benchmarks of nuclear data, particularly the fusion focused ones, through simulations and calculations at FNS[17], [44], [45] and at FNG[22], [59].

Previous studies have been shown that a measurement of neutron energy spectrum was performed by activation analyses using a high purity germanium detector and activation foils[46][60] or using a diamond detector [61], [62] on neutronics experiments irradiated with deuterium-deuterium (DD) fusion neutrons. Although the neutron measuring method using activation foils plans to be installed for ITER with neutron activation system (NAS), the NAS aims for neutron diagnostics at some fixed points (inside TBM, around components)[28]. Since neutron fluxes and spectra are estimated to be broadly distributed inside each blanket module, the estimation for the whole blanket performance is hardly evaluated by point measurements. Evaluating tritium production through activation analyses requires a method of measuring neutron spectrum inside the blanket.

Related to the above circumstances, the previous studies reported the feasibility of measuring fast and thermal neutron distributions by the collaboration of activation foils and the imaging plate with DD reaction neutrons[63], [64].

This chapter reports the simulation for measuring the neutron distribution focused on specific energy regions inside the blanket mock-up

using activation foils and the imaging plate of 2D radiation dosimeter on the irradiation with 14 MeV neutrons by deuterium-tritium (DT) reactions. Reaction ratios of a manganese foil and a dysprosium foil covered by cadmium foils were simulated for measuring thermal and epi-thermal neutrons. For the optimization of using the imaging plate, required time transitions of cooling, exposure and fading for activation analyses were performed.

4.2 Methods of simulations

Fig. 4–1 shows the simulated configuration of a blanket mock-up. The blanket mock-up was composed of reduced-activation ferritic/martensitic steel F82H, beryllium, lithium compounds, and. Specifically, F82H were selected for the first wall and the structural material, beryllium was selected as a neutron multiplier, lithium titanate (Li_2TiO_3) or lithium carbonate (Li_2CO_3) was selected as a tritium breeder, and polyethylene was selected for substitutions of cooling water. The mock-up was constituted four layers of beryllium and lithium layers repeatedly, and the mock-up was covered with graphite as a neutron reflector. The Table 1 indicates densities of compositions, and especially lithium set by 40% enrichment of ^6Li for Li_2TiO_3, and natural abundant for Li_2CO_3 layers.

Table 4–1 Materials and densities of mock-up compositions.

Structure name	Material	Density g/cm^3
First wall	RAFM (F82H)	7.87
Tritium breeder	Li_2TiO_3 Li_2CO_3	2.01 (59%)* 1.62 (77%)*
Neutron multiplier	Beryllium	1.85 (100%)*
Reflector	Graphite	1.89 (84%)*
Cooling water	Polyethylene	0.95
Foil supporter	Stain-less steel	8.73 (100%)*

*ratio of simulated density to theoretical density

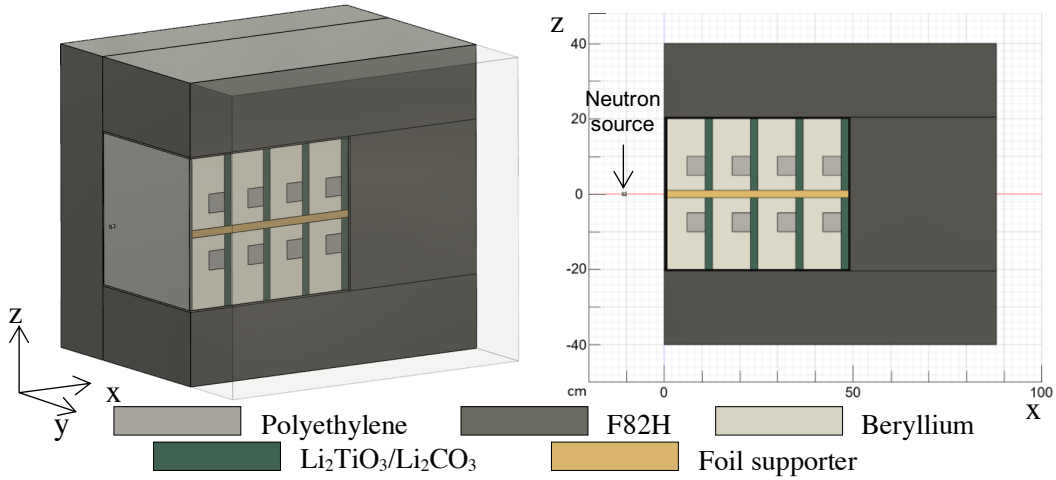

Fig.4–1 The 3D drawing and cross-section of the simulated blanket mock-up configuration

There was an area for the installation of activation foils inside the mock-up. Material foils are planned to be installed with a supporter made of stainless in case of being damaged during actual experiments. Material foils were installed inside the mock-up, shown in Fig.4–1. Foils of gold, indium, dysprosium, manganese, cobalt, and niobium (Au, In, Dy, Mn, Co and Nb) were selected. Each of the activation foils has specifically high reaction region with neutron; Au reacts thermal neutrons and has a peak of 4.89 eV, In reacts thermal neutrons and has a peak of 1.46 eV, Dy reacts thermal neutrons highest among the other foils, Mn reacts epi-thermal (defined as 1.0 to 10^6 eV) and thermal (less than 1.0 eV) neutrons, Co and Nb reacts fast neutrons using (n,2n) reactions which have threshold reactions of 10.7 MeV and 9.1 MeV. In order to measure epi-thermal neutrons, foils of manganese and dysprosium were covered with cadmium (Cd) foils. In this study, each thickness of activation foils was selected below; 0.05 mm for Au and In, 0.25 mm for Dy, 1.00 mm for Mn, 0.40 mm for Co, 2.0 mm for Nb, and 0.5 mm and 1.0 mm for Cd[65].

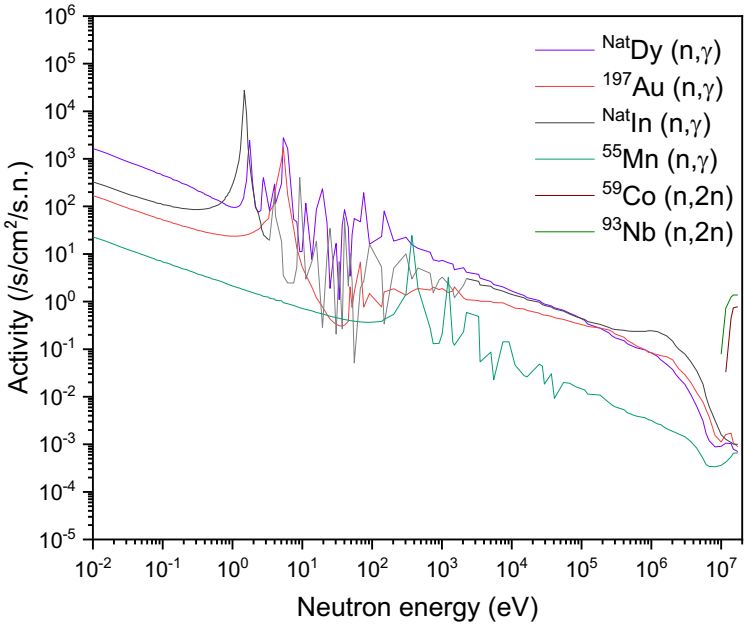

Fig. 4–2 Reaction cross section of the selected materials by JENDL-4.0 [71]

Simulations of the Monte Carlo neutron transport were performed by MCNP6[66] with the nuclear data library ENDF/B-VIII.0[67] and FENDL-3.1d[68]. Neutron source was defined as monochromatic 14.05 MeV neutrons irradiated from a volumetric isotropic source. Simulations were divided into two cases employed by Li_2CO_3 layers and Li_2TiO_3 layers, respectively. For comparisons of each tritium production rate (TPR), lithium was set as natural abundance for Li_2CO_3 and 40% enrichments of ^6Li for Li_2TiO_3.

Simulations of the activation analyses were performed by DCHAIN-SP[38] which is the included package of PHITS[69] with the neutron activation cross section data library FENDL/A-2.0[54]. Duration of neutron irradiation was set for 3 hours, and neutron production rate were set as 10^{10} n/sec. After the irradiation, each activity of generated daughter nuclides was tracked by time.

Considering simulations of generated nuclides with each half-life, cooling time, exposure time, and fading time were set for each of activation foils for measurements using the imaging plate. Cooling time was set for becoming each activity stable, and they were calculated based on half-lives of generated nuclides. Exposure time was set for measuring each activity of

dominant nuclides. Furthermore, it was reported that an imaging plate has the fading effect which decreases the exposure data by time and affects the read-out data[70]. In this study, the fading time (1.5-2.0 hours) was set for the schedule of measurements in order to avoid the fading effect.

4.3 Results

4.3.1 Neutron fluxes inside the blanket mock-up

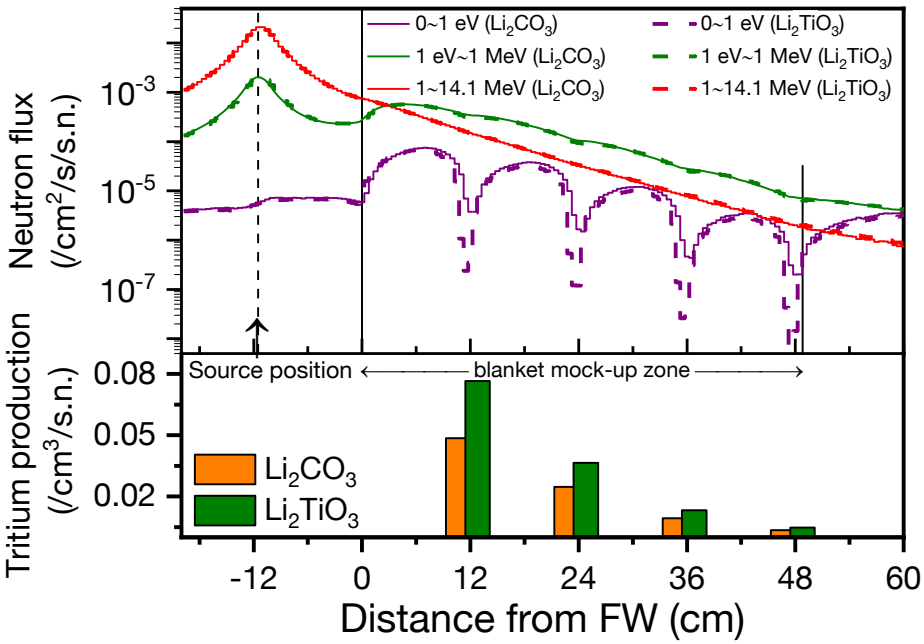

Fig. 4–3 Neutron fluxes and tritium production by distance from the first wall (FW)

As shown in Fig. 4–3, the cross-section of the blanket mock-up, neutron fluxes corresponding to the distance from the first wall to the end of the mock-up and averaged tritium production rates of each lithium layer were obtained. Neutron fluxes were divided into three groups of energy regions: 0 to 1 eV (thermal), 1 eV to 1 MeV (epi-thermal) and 1 to 14.1 MeV (fast) neutrons. Fast neutrons were decreased regarding radially distributing from the centre of the neutron source, and epi-thermal and thermal neutrons were increased by neutron attenuations inside the blanket mock-up. Neutron attenuations were mainly occurred by carbon graphite blocks and Be blocks. Thermal neutrons were increased by 10 to 10^2 times inside each Be layer and decreased by 10 or more than 10^2 inside each Li layer which was occurred

by the reaction of $^{6}Li(n,t)^{4}He$ and $^{7}Li(n,n't)^{4}He$. Each tritium production rate was calculated and averaged by Li layer 1 to 4, and differences of tritium production rates between Li_2CO_3 and Li_2TiO_3 were caused by enrichments of ^{6}Li.

4.3.2 Tritium production

One tritium production rate was averaged each layer as shown in Fig. 4–3. Tritium production rate was gradually decreased by distances and each rate of the Li_2TiO_3 case was about two times as much as the Li_2CO_3 case because of the enrichment.

Though each tritium production rate was obtained and shown in Fig. 4–3, tritium productions differ from the distance between front and rear of each layer[45]. Fig. 4–4 shows the relation of tritium production rate in Li layer 1 integrated by energy regions divided into 3 groups of the $^{6}Li(n,t)^{4}He$ reactions and the $^{7}Li(n,n't)^{4}He$ threshold reaction. As shown in Fig. 4–4, thermal neutrons were dominant for front and rear of layers, and epi-thermal neutrons were dominant for middle, and that tendency was remarkable for the ^{6}Li-enriched Li_2TiO_3. This result indicates that thermal neutrons are mostly captured by the surface of the layer, and epi-thermal neutrons were become dominant in the middle of the layer.

Fig. 4–5 shows the comparison of tritium production rate in each Li layer. Each tritium production rate was high on the front and rear surfaces, and they decreased by one fifth to one tenth about middle. In this result with NPR for 10^{10} n/sec and irradiation duration for 3 hours, two cases of lowest activity of tritium inside Li_2CO_3 and Li_2TiO_3 layer 4 were about 0.035 and 0.070 (Bq/cm3) which were sufficient to measure β-rays by a liquid scintillation counter.

Fig. 4–6 shows the reaction cross section of $^{6}Li(n,t)$ by JENDL-4.0[71], neutron spectrum at the front of Li layer-1, and reaction rate of tritium production at the front and middle of Li layer-1. Cumulative rate of reactions of the thermal region was dominant at the front of Li layer. On the other hand, cumulative rate of reactions of the epi-thermal region was dominant at the middle of Li layer. This difference was caused by absorption of neutrons by reactions of $^{6}Li(n,t)$.

Fig. 4–7 shows the reaction rate of material foils of Mn and Dy and each cumulative ratio of energy regions. The dominant region of Mn was epi-thermal neutrons and the dominant region of Dy was thermal neutrons, which resulted in measuring neutrons by energy regions.

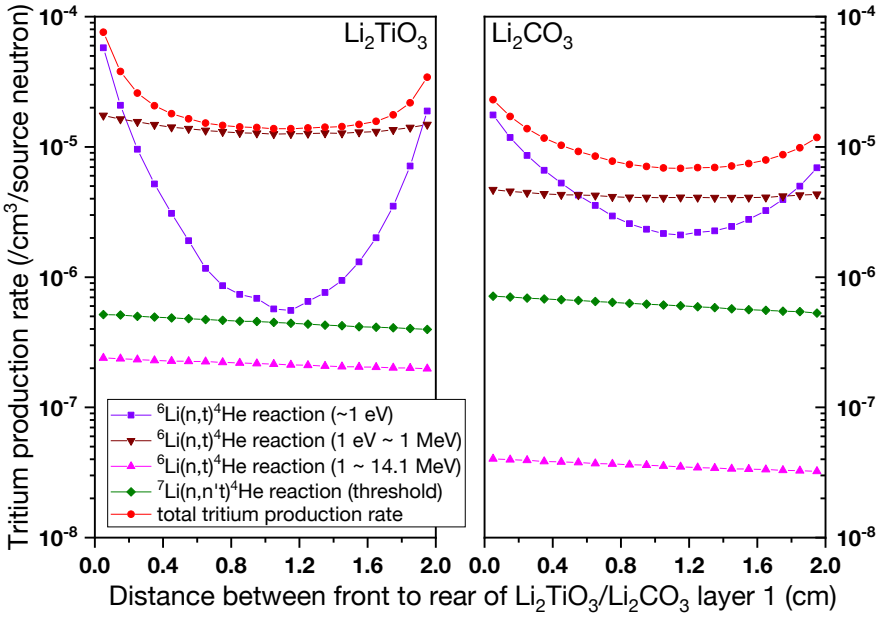

Fig. 4–4 The relations of tritium production rate in Li_2TiO_3 layer 1, and Li_2CO_3 layer 1

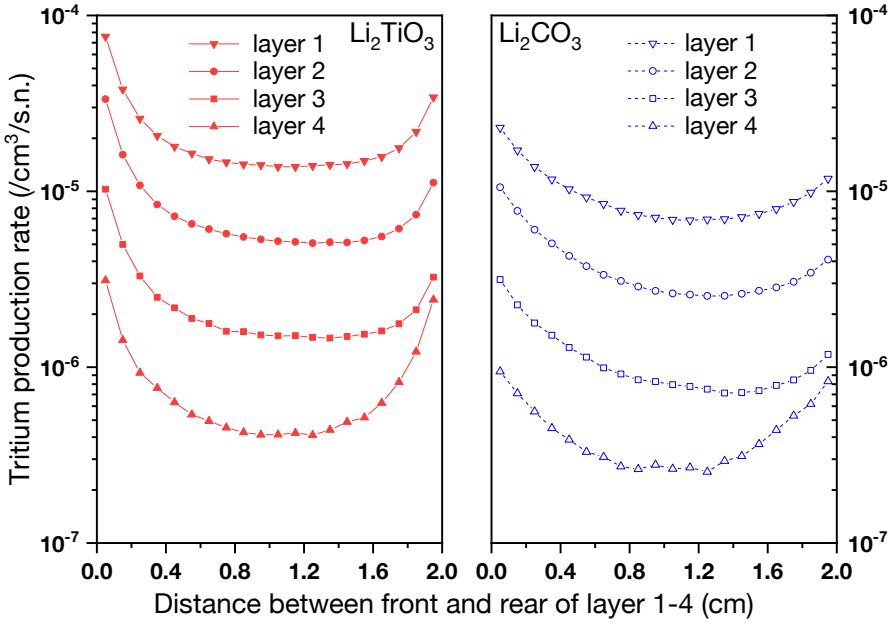

Fig. 4–5 Total tritium production rate inside the layer 1-4

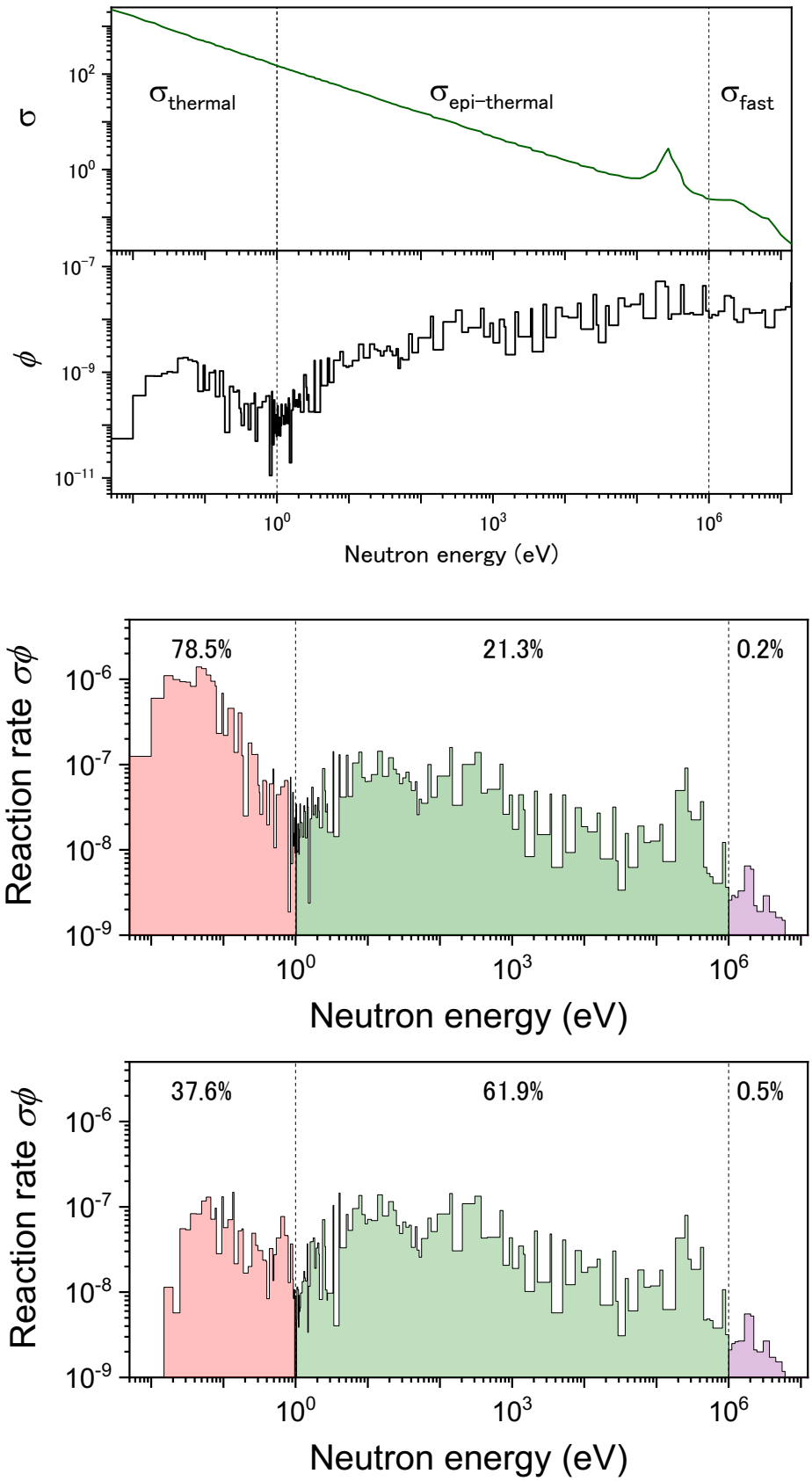

Fig. 4–6 Reaction cross section of ^{6}Li(n,t) (σ), neutron spectrum at the front of Li layer-1, and reaction rate of tritium production at the front and middle of Li layer-1

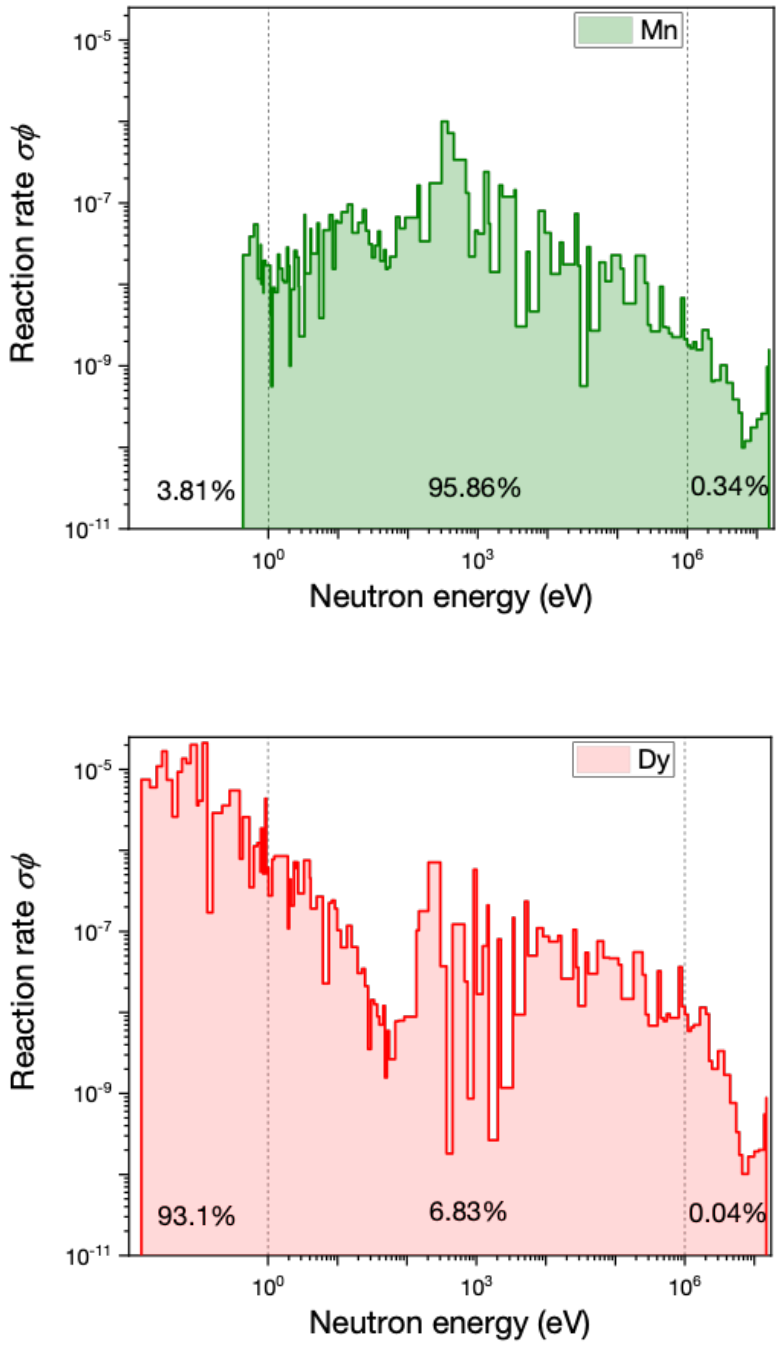

Fig. 4–7 Reaction rate of each material foil of Mn and Dy by (n,γ) reaction divided into 3 energy regions

4.3.3 Effect of covering Mn and Dy with Cd foils

Fig.4–8 shows the neutron spectrum in Mn and Dy foils which are covered by Cd foil or non-covered. In the case of covering, thermal neutrons were captured by Cd and then the reaction rates with thermal neutrons were reduced. Fig.4–9 shows cumulative ratios of (n,γ) reactions of Mn and Dy divided into 3 energy groups of thermal, epi-thermal and fast neutrons. In the case of Mn covered with Cd of 0.5 mm thickness, the reaction rate of Dy with thermal neutrons decreased by 20% compared to non-covering, which resulted in that the dominant neutron energy region of (n,γ) reaction of Mn were shifted to the region of epi-thermal neutrons. Reaction rate of thermal neutrons also decreased by 64% about Dy, and Dy was still reacted with thermal neutrons by 29%. In the case of Mn with Cd covering of 1.0 mm thickness, the reaction rate of thermal neutrons decreased, and the

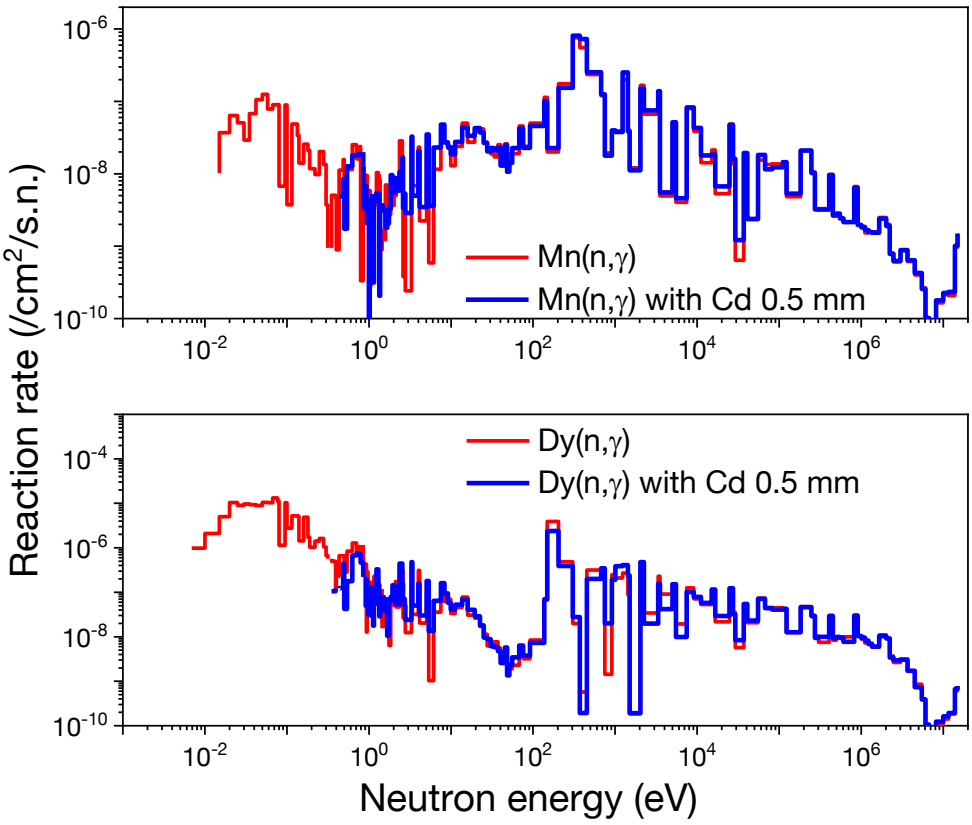

Fig. 4–8 Relationships of Mn(n,γ) and Dy(n,γ) reaction rate with or without Cd coverings

cumulative reaction rate was 98% which was almost same as the case of 0.5 mm thickness. This result indicates that Mn with Cd of 0.5 mm thickness was sufficient for the reaction with epi-thermal neutrons. As shown in Fig. 4–8, tritium production in each Li layer was evaluated by means of Mn with Cd of 0.5–1.0 mm thickness for epi-thermal neutrons and Dy without Cd for thermal neutrons by 0.97–0.98 and 0.93, respectively. For the practical measurement, TBR is required to be more than 1.05 and it should be evaluated with 5–10 % errors from factors of geometries, nuclear data, and statistical errors by calculations, and calibration errors and measured errors by measuring devices. In this work, tritium production in Li-1 layer was feasible to be evaluated with the error of 6.2 % at the front and the error of 4.4 % at the middle.

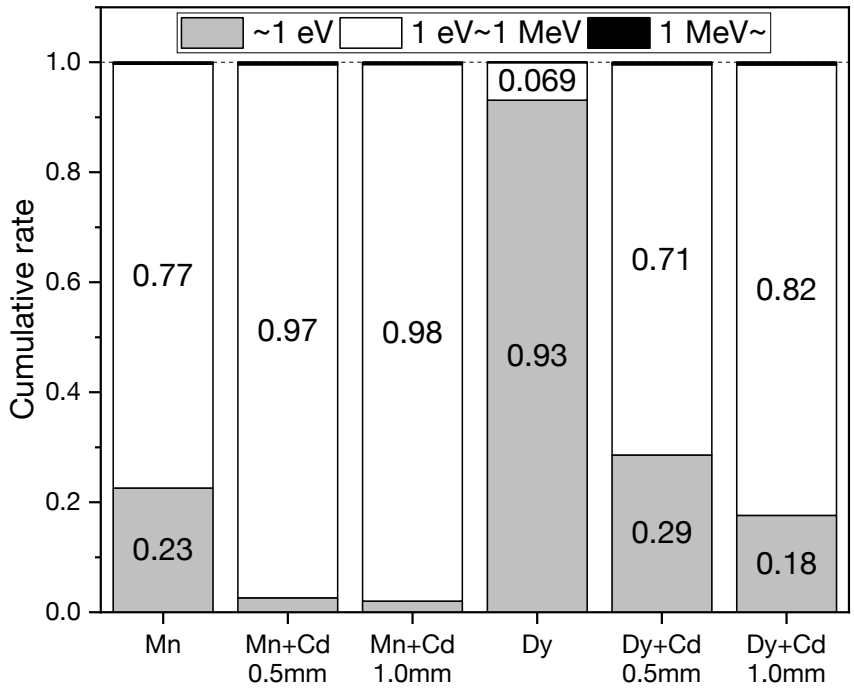

Fig. 4–9 The cumulative ratios of (n, γ) reactions integrated by specific energy regions

4.3.4 Activation simulations for analyses using imaging plate

Fig. 4–10 shows the changes of total activity of the activation foils during and after the neutron irradiation. The activities of Dy, Au, Nb and Co steeply decreased by 1 or 2 digits caused by the generated daughter nuclides with very short half-lives within several seconds. Fig. 4–11 shows ratios of each dominant nuclide to the whole generated nuclides. Since generated short (within minutes) half-life daughter nuclides of Au, In and Dy were shortly decayed, each cooling time was set for half an hour, and dominant daughter nuclides (more than 90% to the whole generated nuclides in this study) became their targets of measurements. ^{198}Au of the dominant daughter nuclide has a half-life of 2.69 days. ^{116m}In which has a half-life of 54.3 minutes was the dominant daughter nuclide for 6 hours after irradiation, and the ratio steeply descended. ^{165}Dy of the dominant daughter nuclide has a half-life of 2.33 hours, and ^{165}Dy kept dominant after irradiation. 56Mn of the dominant daughter nuclide has a half-life of 2.58 hours, and ^{56}Mn kept dominant after irradiation. Nb and Co generated daughter nuclides of ^{94m}Nb and ^{60m}Co whose half-lives are 6.26 minutes and 10.5 minutes, respectively. ^{58m}Co became dominant for 2 hours after the irradiation, and ^{92m}Nb became dominant for 7 hours after the irradiation.

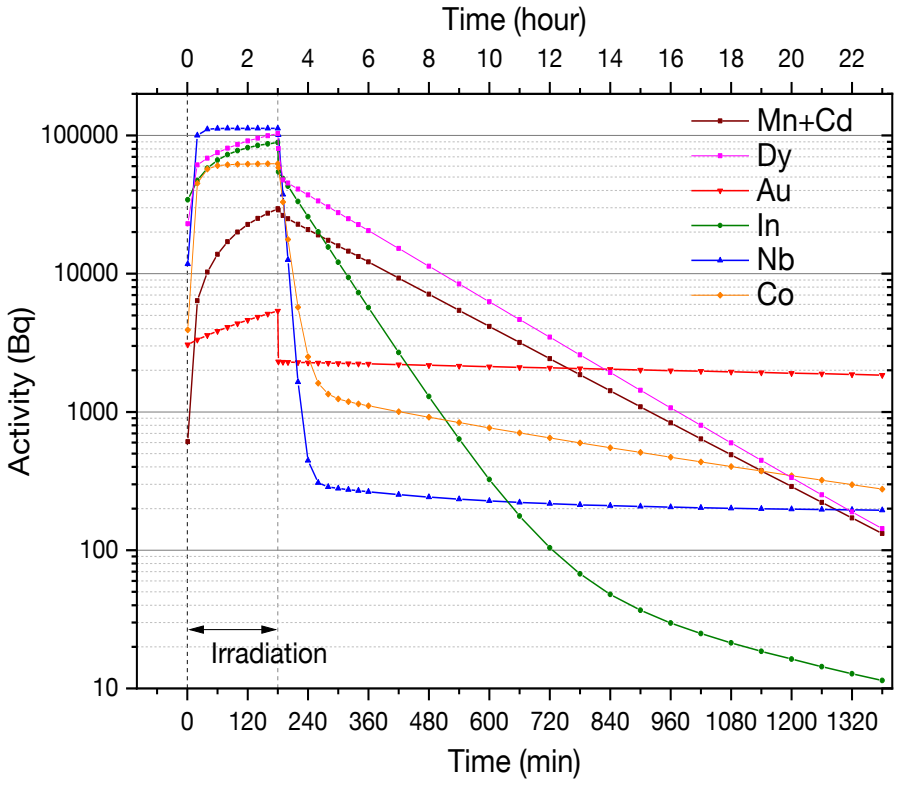

Fig. 4–10 Relations between activities and time of irradiated activation foils

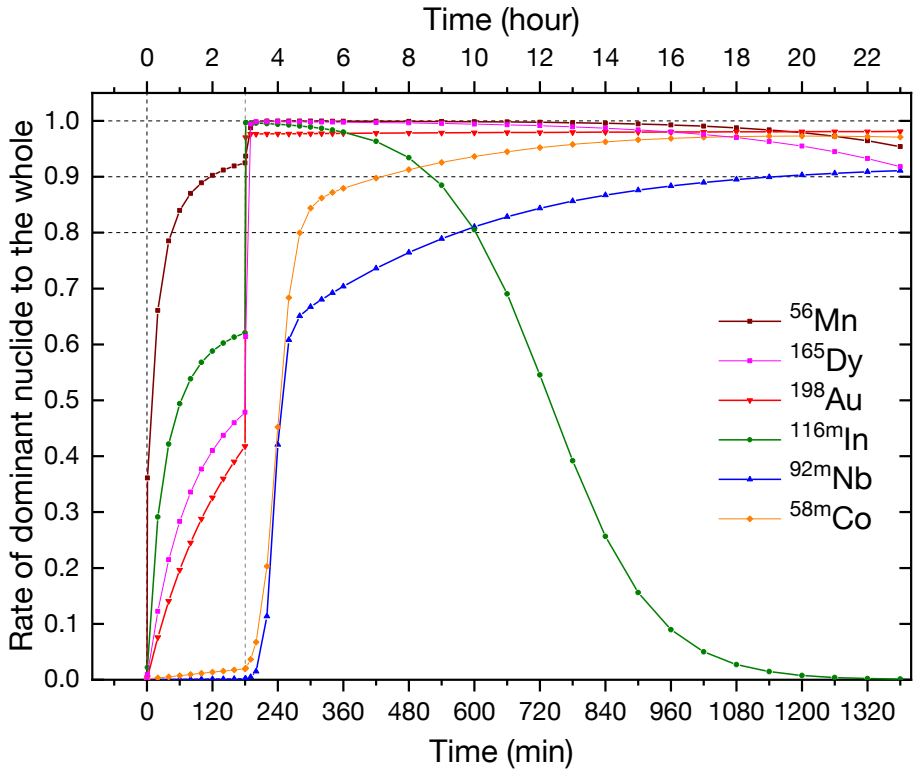

Fig. 4–11 Relations between rates of dominant nuclides to the whole generated nuclides and time

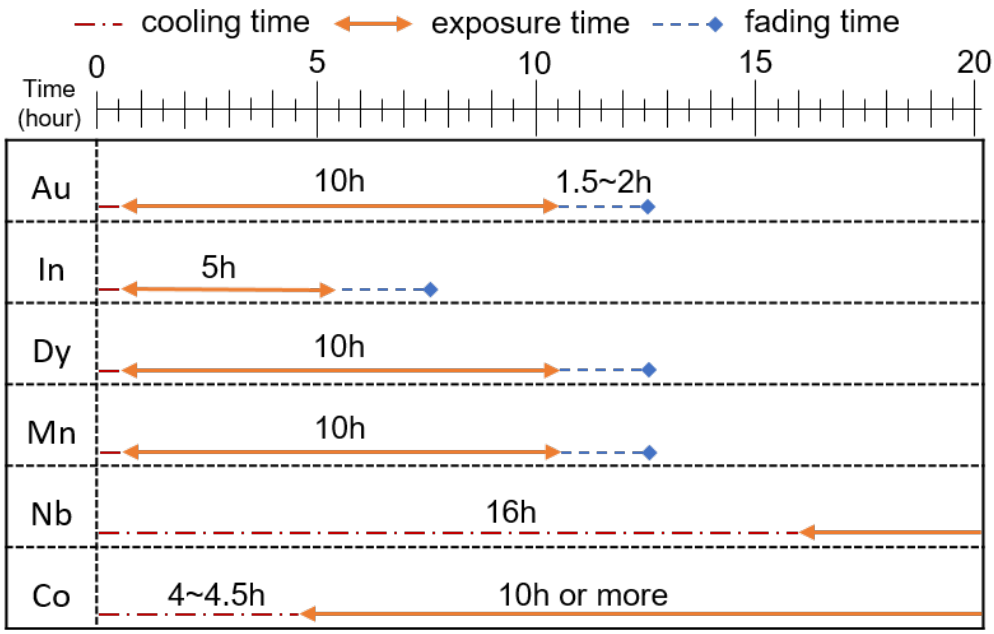

Fig. 4–12 The estimated schedule for the activation analysis using activation foils and the imaging plate

Fig. 4–12 shows an estimated schedule applied for actual activation analyses using the imaging plate. Since generated short (within minutes) half-life daughter nuclides of Au, In and Dy were shortly decayed, each cooling time was set for half an hour. ^{116m}In, the dominant nuclide of In, kept dominant (more than 90%) for 5 hours after irradiation. To avoid decreasing the ratio of the dominant nuclide, the exposure time was set for 5 hours. In the case of Nb and Co, each cooling time was required to set more time than other materials. Since activities of Nb and Co were lower than other materials, each exposure time was required to set for 10 or more hours.

Based on these results, Dy, Au, Mn and Co were promising candidates for the measurement using imaging plate because dominant nuclides were stable. The dominant nuclides of In and Nb were largely changed after the irradiation, which seems to affect the measuring data of the imaging plate.

4.4 Conclusions of Chapter 4

In this chapter, the simulation for the neutron measurement inside the blanket mock-up was performed. The simulated results of neutron transport and activation analyses indicate followings:

Based on the results of the activation analysis, neutron yield of 10^{10} n/sec. was sufficient for the measurement of activation foils installed inside a blanket mock-up using the imaging plate.

Neutron attenuation inside Be and Li layers and tritium production inside Li layers were confirmed, and detailed tritium production rate were calculated. Tritium production was dominantly caused with thermal neutrons on the surface of Li layer, while epi-thermal neutrons was dominant in the middle of the layer. This result proposes the requirement of measuring thermal and epi-thermal neutron fluxes inside the Li layer for the evaluation of TBR.

The foil activation method was the candidate for measuring neutrons divided into 3 groups of energy regions; especially, the Mn foil with Cd covering was suggested to measure the epi-thermal neutron region. Dy was not for measuring the epi-thermal neutrons but for thermal neutrons.

Simulated results of activation analyses indicate the feasibility of measuring neutrons using an imaging plate and activation foils. The activation analysis using the imaging plate and activation foils of Dy, Au, Mn with Cd and Co are candidates for the evaluation of spatial neutron distribution inside the blanket mock-up.

5. Conclusions and future works

Chapter 1 introduced the background of energy problems in Japan and on the whole world and the approaches of the fusion reactor for solving these problems. Then, requirements of neutronics experiments for the development of blanket systems were introduced, and current issues of measurement of neutron and tritium were summarised.

In Chapter 2 and Chapter 3, novel methods of measuring spatial neutron distribution divided into specific energy regions were proposed. Employing the imaging plate and material foils, neutron fluxes were obtained divided into thermal and epi-thermal neutrons regarding the reaction cross section of each material. The spatial distribution of neutron fluxes inside the blanket mock-up was feasible to be measured by 0.5 cm interval and to be separated by energy regions using the imaging plate and the combination of material foils.

In Chapter 4, the preliminary result of an actual experiment to measure spatial distribution divided into specific energy regions of thermal, epi-thermal, and fast neutrons was obtained considering the neutron irradiation by deuterium-tritium (DT) fusion reactions inside the blanket mock-up. Installing material foils inside the mock-up, neutron fluxes were obtained by energy regions and time transitions of using the imaging plate and the combination of materials were simulated and calculated through the activation analysis. Tritium production inside the mock-up was also calculated, and dominant region of neutron energy was different among the breeding layers. Selected material foils were confirmed to be employed for the measurement of each energy region of neutrons.

Based on these results, the neutron distribution divided into energy regions is feasible to be measured inside the blanket, and this method is also feasible to be applied for measuring tritium production.

For the future study, the actual experiment irradiating DT neutrons is required, and the accuracy of the measurement value obtained by the IP is required to be improved.

Appendix: Energy group structure

Energy group structure of XMAS LWPC 172-group structure[72] was employed for the simulation and evaluation of neutron fluxes.

Division number	Neutron energy (MeV)	Division number	Neutron energy (MeV)
1	1.00E-11	33	4.00E-07
2	3.00E-09	34	4.33E-07
3	5.00E-09	35	4.85E-07
4	6.90E-09	36	5.00E-07
5	1.00E-08	37	5.40E-07
6	1.50E-08	38	6.25E-07
7	2.00E-08	39	7.05E-07
8	2.50E-08	40	7.80E-07
9	3.00E-08	41	7.90E-07
10	3.50E-08	42	8.50E-07
11	4.20E-08	43	8.60E-07
12	5.00E-08	44	9.10E-07
13	5.80E-08	45	9.30E-07
14	6.70E-08	46	9.50E-07
15	7.70E-08	47	9.72E-07
16	8.00E-08	48	9.86E-07
17	9.50E-08	49	9.96E-07
18	1.00E-07	50	1.02E-06
19	1.15E-07	51	1.04E-06
20	1.34E-07	52	1.05E-06
21	1.40E-07	53	1.07E-06
22	1.60E-07	54	1.10E-06
23	1.80E-07	55	1.11E-06
24	1.89E-07	56	1.13E-06
25	2.20E-07	57	1.15E-06
26	2.48E-07	58	1.17E-06
27	2.80E-07	59	1.24E-06
28	3.00E-07	60	1.30E-06
29	3.15E-07	61	1.34E-06
30	3.20E-07	62	1.37E-06
31	3.50E-07	63	1.44E-06
32	3.91E-07	64	1.48E-06

Division number	Neutron energy (MeV)	Division number	Neutron energy (MeV)
65	1.50E-06	97	3.05E-05
66	1.59E-06	98	3.37E-05
67	1.67E-06	99	3.73E-05
68	1.76E-06	100	4.02E-05
69	1.84E-06	101	4.55E-05
70	1.93E-06	102	4.83E-05
71	2.02E-06	103	5.16E-05
72	2.10E-06	104	5.56E-05
73	2.13E-06	105	6.79E-05
74	2.36E-06	106	7.57E-05
75	2.55E-06	107	9.17E-05
76	2.60E-06	108	1.37E-04
77	2.72E-06	109	1.49E-04
78	2.77E-06	110	2.04E-04
79	3.30E-06	111	3.04E-04
80	3.38E-06	112	3.72E-04
81	4.00E-06	113	4.54E-04
82	4.13E-06	114	6.77E-04
83	5.04E-06	115	7.49E-04
84	5.35E-06	116	9.14E-04
85	6.16E-06	117	1.01E-03
86	7.52E-06	118	1.23E-03
87	8.32E-06	119	1.43E-03
88	9.19E-06	120	1.51E-03
89	9.91E-06	121	2.03E-03
90	1.12E-05	122	2.25E-03
91	1.37E-05	123	3.35E-03
92	1.59E-05	124	3.53E-03
93	1.95E-05	125	5.00E-03
94	2.26E-05	126	5.53E-03
95	2.50E-05	127	7.47E-03
96	2.76E-05	128	9.12E-03

Division number	Neutron energy (MeV)	Division number	Neutron energy (MeV)
129	1.11E-02	161	3.01E+00
130	1.50E-02	162	3.68E+00
131	1.66E-02	163	4.49E+00
132	2.48E-02	164	5.49E+00
133	2.74E-02	165	6.07E+00
134	2.93E-02	166	6.70E+00
135	3.70E-02	167	8.19E+00
136	4.09E-02	168	1.00E+01
137	5.52E-02	169	1.16E+01
138	6.74E-02	170	1.38E+01
139	8.23E-02	171	1.49E+01
140	1.11E-01	172	1.73E+01
141	1.23E-01	173	1.96E+01
142	1.83E-01		
143	2.47E-01		
144	2.73E-01		
145	3.02E-01		
146	4.08E-01		
147	4.50E-01		
148	4.98E-01		
149	5.50E-01		
150	6.08E-01		
151	8.21E-01		
152	9.07E-01		
153	1.00E+00		
154	1.11E+00		
155	1.22E+00		
156	1.35E+00		
157	1.65E+00		
158	2.02E+00		
159	2.23E+00		
160	2.47E+00		

References

[1] N. Craik, "Developing a National Strategy for Climate Engineering Research in Canada," *Clim. Eng.*, no. 153, p. 24, 2017.

[2] B. M. Sanderson, B. C. O'Neill, and C. Tebaldi, "What would it take to achieve the Paris temperature targets?," *Geophys. Res. Lett.*, vol. 43, no. 13, pp. 7133–7142, 2016, doi: 10.1002/2016GL069563.

[3] U. Shumlak, "Z-pinch fusion," *J. Appl. Phys.*, vol. 127, no. 20, p. 200901, 2020, doi: 10.1063/5.0004228.

[4] A. Sykes *et al.*, "Compact fusion energy based on the spherical tokamak," *Nucl. Fusion*, vol. 58, no. 1, 2018, doi: 10.1088/1741-4326/aa8c8d.

[5] M. J. Moynihan, "Fusion Chart." https://thefusionblog.quora.com/Citations-For-Fusion-Chart (accessed Dec. 18, 2021).

[6] T. Fujita *et al.*, "High performance experiments in JT-60U reversed shear discharges," *Nucl. Fusion*, vol. 39, no. Special Issu, pp. 1627–1636, 1999, doi: 10.1088/0029-5515/39/11Y/302.

[7] Y. Someya *et al.*, "Design study of blanket structure based on a water-cooled solid breeder for DEMO," *Fusion Eng. Des.*, vol. 98–99, pp. 1872–1875, 2015, doi: 10.1016/j.fusengdes.2015.05.042.

[8] S. Konishi *et al.*, "Functional materials for breeding blankets—status and developments," *Nucl. Fusion*, vol. 57, no. 9, p. 092014, Sep. 2017, doi: 10.1088/1741-4326/aa7e4e.

[9] G. W. Bailey, O. V. Vilkhivskaya, and M. R. Gilbert, "Waste expectations of fusion steels under current waste repository criteria," *Nucl. Fusion*, vol. 61, no. 3, 2021, doi: 10.1088/1741-4326/abc933.

[10] M. Nishikawa, K. I. Tanaka, and M. Uetake, "Study on a method to recover tritium from blanket sweep gas," *Fusion Technol.*, vol. 26, no. 1, pp. 17–26, 1994, doi: 10.13182/FST94-A30298.

[11] M. Enoeda *et al.*, "Development of the Water Cooled Ceramic Breeder Test Blanket Module in Japan," *Fusion Eng. Des.*, vol. 87, no. 7–8, pp. 1363–1369, Aug. 2012, doi: 10.1016/J.FUSENGDES.2012.03.007.

[12] W. Guan *et al.*, "Creep-fatigue interaction on estimation of lifetime and fatigue damage of F82H," *Fusion Eng. Des.*, vol. 173, p. 112830, Dec. 2021, doi: 10.1016/J.FUSENGDES.2021.112830.

[13] Y. Kawamura *et al.*, "Progress of water cooled ceramic breeder test blanket module system," *Fusion Eng. Des.*, vol. 161, no. October 2019, p. 112050, 2020, doi: 10.1016/j.fusengdes.2020.112050.

[14] U. Fischer *et al.*, "Required, achievable and target TBR for the European DEMO," *Fusion Eng. Des.*, vol. 155, no. February, p. 111553, 2020, doi: 10.1016/j.fusengdes.2020.111553.
[15] Y. Someya, K. Tobita, R. Hiwatari, and Y. Sakamoto, "Fusion DEMO reactor design based on nuclear analysis," *Fusion Eng. Des.*, vol. 136, pp. 1306–1312, Nov. 2018, doi: 10.1016/J.FUSENGDES.2018.04.129.
[16] S. Sato *et al.*, "Neutronics experiments for DEMO blanket at JAERI/FNS," *Nucl. Fusion*, vol. 43, no. 7, pp. 527–530, 2003, doi: 10.1088/0029-5515/43/7/303.
[17] S. Sato *et al.*, "Neutronics experimental study on tritium production in solid breeder blanket mockup with neutron reflector," *J. Nucl. Sci. Technol.*, vol. 44, no. 4, pp. 657–663, 2007, doi: 10.1080/18811248.2007.9711854.
[18] A. Klix, "Blanket Experiments Using Enriched Li2Tior/Ferritic Steel/Beryllium Assemblies and D-T Fusion Neutrons," *Plasma fusion Res.*, vol. 5, pp. 565–569, 2002.
[19] C. M. Logan and D. W. Heikkinen, "RTNS-II - a fusion materials research tool," *Nucl. Instruments Methods Phys. Res.*, vol. 200, no. 1, pp. 105–111, Sep. 1982, doi: 10.1016/0167-5087(82)90518-X.
[20] S. Sato *et al.*, "Conceptual design of advanced fusion neutron source (A-FNS) and irradiation test modules," *Nucl. Fusion*, vol. 61, no. 10, 2021, doi: 10.1088/1741-4326/ac21f6.
[21] M. Ohta *et al.*, "Conceptual design of test modules for DEMO blanket, diagnostic device, and RI production for A-FNS," *Fusion Eng. Des.*, vol. 157, no. September 2019, p. 111632, 2020, doi: 10.1016/j.fusengdes.2020.111632.
[22] A. Pietropaolo *et al.*, "The Frascati Neutron Generator: A multipurpose facility for physics and engineering," *J. Phys. Conf. Ser.*, vol. 1021, no. 1, 2018, doi: 10.1088/1742-6596/1021/1/012004.
[23] M. Martone, M. Angelone, and M. Pillon, "The 14 MeV Frascati neutron generator," *J. Nucl. Mater.*, vol. 212–215, no. PART B, pp. 1661–1664, 1994, doi: 10.1016/0022-3115(94)91109-6.
[24] J. C. Sublet, M. Fleming, and M. R. Gilbert, "From cutting-edge pointwise cross-section to groupwise reaction rate: A primer," *EPJ Web Conf.*, vol. 146, 2017, doi: 10.1051/epjconf/201714602003.
[25] S. P. Simakov, A. Koning, and A. Y. Konobeyev, "Covariances for the 56Fe radiation damage cross sections," *EPJ Web Conf.*, vol. 146, 2017, doi: 10.1051/epjconf/201714602012.
[26] S. K. Michinori Yamauchi, Takeo Nishitani, Kentaro Ochiai, Yuichi Morimoto, Jun-ichi Hori, Katsuyuki Ebisawa, "Performance test of micro-fission chambers for in-vessel neutron monitoring of ITER,"

2002.
[27] J. R. D. Copley and T. J. Udovic, “Neutron Time-of-Flight Spectroscopy,” 1993.
[28] L. Bertalot *et al*., “Fusion neutron diagnostics on ITER tokamak,” *J. Instrum*., vol. 7, no. 4, 2012, doi: 10.1088/1748-0221/7/04/C04012.
[29] K. Ochiai *et al*., “DESIGN PROGRESS OF ADVANCED FUSION NEUTRON SOURCE FOR JA / DEMO FUSION REACTOR,” pp. 1–8.
[30] K. Noborio, Y. Yamamoto, and S. Konishi, “Optimizing the electrode configuration of a cylindrical discharge-type fusion device by computational and experimental analysis,” *Plasma Fusion Res*., vol. 9, pp. 1–4, 2014, doi: 10.1585/pfr.9.1306142.
[31] T. Kanagae, K. Noborio, Y. Yamamoto, and S. Konishi, *Generation of neutron beam by the cylindrical discharge fusion device; Generation of neutron beam by the cylindrical discharge fusion device*. 2009.
[32] M. Kobayashi *et al*., “First measurements of thermal neutron distribution in the LHD torus hall generated by deuterium experiments,” *Fusion Eng. Des*., 2018, doi: 10.1016/j.fusengdes.2018.09.013.
[33] X.-5 M. C. Team, “MCNP-A General Monte Carlo N-Particle Transport Code, Version 5.” Los Alamos National Laboratory, Los Alamos, 2008.
[34] M. B. Chadwick *et al*., “ENDF/B-VII.1 Nuclear Data for Science and Technology: Cross Sections, Covariances, Fission Product Yields and Decay Data,” *Nucl. Data Sheets*, vol. 112, no. 12, pp. 2887–2996, Dec. 2011, doi: 10.1016/J.NDS.2011.11.002.
[35] “Nuclear Data Libraries for Advanced Systems-Fusion Devices (FENDL-3.0),” Vienna, Austria, 2011.
[36] R. P.-C. L. R. Greenwood, “Summary Report of the Technical Meeting on International Reactor Dosimetry File: IRDF-2002,” 2002.
[37] N. Y. S. Chiba, T. Fukahori, K. Shibata, B. Yu, K. Kosako, “JENDL fusion file 99,” *J. Nucl. Sci. Technol*., vol. 39, pp. 187–194, 2002.
[38] T. Kai, F. Maekawa, K. Kosako, Y. Kasugai, H. Takada, and Y. Ikeda, “DCHAIN-SP 2001: High Energy Particle Induced Radioactivity Calculation Code,” *JAERI-Data/Code 2001-016*. 2001.
[39] A. L. Meadowcroft, C. D. Bentley, and E. N. Stott, “Evaluation of the sensitivity and fading characteristics of an image plate system for x-ray diagnostics,” *Rev. Sci. Instrum*., vol. 79, no. 11, pp. 1–5, 2008, doi: 10.1063/1.3013123.
[40] H. Kobayashi and M. Satoh, “Basic performance of a neutron sensitive photostimulated luminescence device for neutron radiography,” *Nucl. Instruments Methods Phys. Res. Sect. A Accel. Spectrometers, Detect.*

Assoc. Equip., 1999, doi: 10.1016/S0168-9002(98)01325-4.
[41] K. Mukai and S. Konishi, "Preparation for a neutronics experiment using a discharge fusion device and an imaging plate neutron detector," *Fusion Eng. Des.*, vol. 146, pp. 1633–1636, 2019, doi: 10.1016/j.fusengdes.2019.03.005.
[42] Y. Karasawa Haga, S. Kumazawa, and N. Niimura, "Gamma-ray sensitivity and shielding of a neutron imaging plate," *J. Appl. Crystallogr.*, vol. 32, no. 5, pp. 878–882, 1999, doi: 10.1107/s0021889899005701.
[43] A. Taniyama, D. Shindo, and T. Oikawa, "Detective quantum efficiency of the 25 μm pixel size imaging plate for transmission electron microscopes," *J. Electron Microsc. (Tokyo).*, vol. 46, no. 4, pp. 303–310, 1997, doi: 10.1093/oxfordjournals.jmicro.a023523.
[44] S. Sato *et al.*, "Progress in the blanket neutronics experiments at JAERI/FNS," *Fusion Eng. Des.*, vol. 81, no. 8-14 PART B, pp. 1183–1193, 2006, doi: 10.1016/j.fusengdes.2005.09.078.
[45] S. Sato *et al.*, "Measurement of tritium production rate in water cooled pebble bed multi-layered blanket mockup by DT neutron irradiation experiment," *Nucl. Fusion*, vol. 47, no. 7, pp. 517–521, 2007, doi: 10.1088/0029-5515/47/7/003.
[46] K. Ochiai *et al.*, "Neutron Flux Measurements in ITER-TBM Simulating Assemblies by means of Multi-Foil Activation Method," *Prog. Nucl. Sci. Technol.*, vol. 1, pp. 142–145, 2011.
[47] L. Bertalot *et al.*, "Present Status of ITER Neutron Diagnostics Development," *J. Fusion Energy*, vol. 38, no. 3–4, pp. 283–290, 2019, doi: 10.1007/s10894-019-00220-w.
[48] M. Bakr, K. Masuda, and M. Yoshida, "Improvement of the Neutron Production Rate of IEC Fusion Device by the Fusion Reaction on the Inner Surface of the IEC Chamber," *Fusion Sci. Technol.*, vol. 75, no. 6, pp. 479–486, 2019, doi: 10.1080/15361055.2019.1609821.
[49] K. Masuda, "Nuclear Fusion Based Neutron Sources核融合中性子源," *Hamon*, vol. 27, no. 3, pp. 113–116, 2017, doi: 10.5611/hamon.27.3_113.
[50] G. Boutoux *et al.*, "Study of imaging plate detector sensitivity to 5-18 MeV electrons," *Rev. Sci. Instrum.*, vol. 86, no. 11, 2015, doi: 10.1063/1.4936141.
[51] H. Ohuchi, A. Yamadera, and M. Baba, "Development of a new passive integral dosemeter for gamma ray monitoring using an imaging plate," *Radiat. Prot. Dosimetry*, vol. 107, no. 4, pp. 239–246, 2003, doi: 10.1093/oxfordjournals.rpd.a006396.
[52] T. Sato *et al.*, "Features of Particle and Heavy Ion Transport code

System (PHITS) version 3.02," *J. Nucl. Sci. Technol.*, vol. 55, no. 6, pp. 684–690, Jun. 2018, doi: 10.1080/00223131.2017.1419890.

[53] JAERI, "JAERI-1250 DCHAIN:放射性ならびに安定核種の生成崩壊解析コード," 1977.

[54] A. B. Pashchenko, H. Wienke, J. Kopecky, J. C. S. Sublet, and R. A. Forrest, "FENDL/A-20 Neutron activation cross section data library for fusion applications," International Atomic Energy Agency (IAEA), 1997. [Online]. Available: http://inis.iaea.org/search/search.aspx?orig_q=RN:30022805.

[55] M. Enoeda *et al.*, "Design and technology development of solid breeder blanket cooled by supercritical water in Japan," *Nucl. Fusion*, vol. 43, no. 12, pp. 1837–1844, 2003, doi: 10.1088/0029-5515/43/12/026.

[56] U. Fischer *et al.*, "Required, achievable and target TBR for the European DEMO," *Fusion Eng. Des.*, vol. 155, no. August 2019, p. 111553, 2020, doi: 10.1016/j.fusengdes.2020.111553.

[57] U. Fischer, C. Bachmann, I. Palermo, P. Pereslavtsev, and R. Villari, "Neutronics requirements for a DEMO fusion power plant," *Fusion Eng. Des.*, vol. 98–99, pp. 2134–2137, 2015, doi: 10.1016/j.fusengdes.2015.02.029.

[58] P. Pereslavtsev, F. A. Hernández, G. Zhou, L. Lu, C. Wegmann, and U. Fischer, "Nuclear analyses of solid breeder blanket options for DEMO: Status, challenges and outlook," *Fusion Eng. Des.*, vol. 146, no. September 2018, pp. 563–567, 2019, doi: 10.1016/j.fusengdes.2019.01.023.

[59] D. Flammini *et al.*, "Pre-analysis of the WCLL breeding blanket mock-up neutronics experiment at the frascati neutron generator," *Fusion Eng. Des.*, vol. 156, no. September 2019, p. 111600, 2020, doi: 10.1016/j.fusengdes.2020.111600.

[60] A. Klix, A. Domula, U. Fischer, D. Gehre, G. Kleizer, and I. Rovni, "Preliminary experimental test of activation foil materials with short half-lives for neutron spectrum measurements in the iter tbm," *Fusion Sci. Technol.*, vol. 64, no. 3, pp. 604–612, 2013, doi: 10.13182/FST13-A19159.

[61] M. I. Kobayashi *et al.*, "Thermal neutron measurement by single crystal CVD diamond detector applied with the pulse shape discrimination during deuterium plasma experiment in LHD," *Fusion Eng. Des.*, vol. 161, p. 112063, 2020, doi: https://doi.org/10.1016/j.fusengdes.2020.112063.

[62] K. Mukai *et al.*, "Evaluation of tritium production rate in a blanket mock-up using a compact fusion neutron source," *Nucl. Fusion*, 2021,

[Online]. Available: http://iopscience.iop.org/article/10.1088/1741-4326/abe4e7.
[63] Y. Ogino, K. Mukai, J. Yagi, and S. Konishi, "Preliminary Results of Neutron Transport in Blanket Module by MCNP with Profile Analysis Using Imaging Plate," *Fusion Sci. Technol.*, vol. 75, no. 6, pp. 487–492, 2019, doi: 10.1080/15361055.2019.1611343.
[64] M. Kobayashi *et al.*, "Neutron flux distributions in the Large Helical Device torus hall evaluated by an imaging plate technique in the first campaign of the deuterium plasma experiment," *Nucl. Fusion*, vol. 59, no. 12, 2019, doi: 10.1088/1741-4326/ab3d14.
[65] I. Kodeli *et al.*, "Activation of Mn, Li2O and LiF in the JSI TRIGA reactor to study potential tritium production monitors for fusion applications," *Nucl. Fusion*, vol. 59, no. 8, 2019, doi: 10.1088/1741-4326/ab2256.
[66] T. Goorley *et al.*, "Initial MCNP6 release overview," *Nucl. Technol.*, vol. 180, no. 3, pp. 298–315, 2012, doi: 10.13182/NT11-135.
[67] D. A. Brown *et al.*, "ENDF/B-VIII.0: The 8th Major Release of the Nuclear Reaction Data Library with CIELO-project Cross Sections, New Standards and Thermal Scattering Data," *Nucl. Data Sheets*, vol. 148, pp. 1–142, 2018, doi: 10.1016/j.nds.2018.02.001.
[68] I. Atomic and E. Agency, "INDC International Nuclear Data Committee Nuclear Data Libraries for Advanced Systems- Fusion Devices."
[69] K. J. Cook *et al.*, "Halo Structure of the Neutron-Dripline Nucleus B 19," *Phys. Rev. Lett.*, vol. 124, no. 21, p. 212503, 2020, doi: 10.1103/PhysRevLett.124.212503.
[70] K. A. Tanaka *et al.*, "Calibration of imaging plate for high energy electron spectrometer," *Rev. Sci. Instrum.*, vol. 76, no. 1, p. 013507, 2005, doi: 10.1063/1.1824371.
[71] K. SHIBATA *et al.*, "JENDL-4.0: A New Library for Nuclear Science and Engineering," *J. Nucl. Sci. Technol.*, vol. 48, no. 1, pp. 1–30, Jan. 2011, doi: 10.1080/18811248.2011.9711675.
[72] "XMAS LWPC 172-group structure." http://serpent.vtt.fi/mediawiki/index.php/XMAS_LWPC_172-group_structure (accessed Feb. 01, 2022).

List of figures and tables

Figures

Chapter 1

Chapter 2

Chapter 3

Chapter 4

Tables

Acknowledgements

I would like to thank the members of my dissertation committee Associate Professor J. Yagi, Professor K. Nagasaki, and Professor S. Konishi for their scientific advice, help and support during this work. I would also be given to the team of undergraduate students who helped me complete this work. From back left to right and right front to left front in the photograph: Associate Professor Juro Yagi, the author of this thesis, Assistant Professor Keisuke Mukai, Hiroyuki Tamiya, Shuhei Yamaguchi, Yuto Murata, Shunsuke Kenjo, Takumi Matsuo, Mahmoud Bakr, Toshiro Sakabe, Ryo Omura, Naoto Iwamatsu, and Prof. Satoshi Konishi.

This work was supported by a Grant-in-Aid for Japan Society for the Promotion of Science (JSPS) Fellows (21J15893).

List of publications and presentations

PUBLICATIONS

Yasuyuki Ogino, Keisuke Mukai, Juro Yagi and Satoshi Konishi, "Simulations for practical measurement methods of spatial neutron distribution inside blanket mock-up irradiated with DT neutrons." *Fusion Engineering and Design*, 2021. 168: 112417.

Yasuyuki Ogino, Keisuke Mukai, Juro Yagi and Satoshi Konishi, "Preliminary Results of Neutron Transport in Blanket Module by MCNP with Profile Analysis Using Imaging Plate." *Fusion Science and Technology*, 2019. 75: pp. 487-492.

Yasuyuki Ogino, Shunsuke Kenjo, Toshiro Sakabe, Keisuke Mukai, Mahmoud Bakr, Juro Yagi, and Satoshi Konishi, "Measurements of neutron spatial distribution divided into specific energy regions inside a blanket mock-up." *IEEE Transactions on Plasma Science* (under review)

Shunsuke Kenjo, Yasuyuki Ogino, Keisuke Mukai, Mahmoud Bakr, Juro Yagi, and Satoshi Konishi, "Employing of ZrCo as a fuel source in a discharge-type fusion neutron source operated in self-sufficient mode." *International Journal of Hydrogen Energy*, 2022. 47 no.5: pp. 3054–3062.

Keisuke Mukai, Yasuyuki Ogino, Makoto Kobayashi, Mahmoud Bakr, Juro Yagi, Kunihiro Ogawa, Mitsutaka Isobe and Satoshi Konishi, "Evaluation of tritium production rate in a blanket mock-up using a compact fusion neutron source." *Nuclear Fusion*, 2021. 61: 046034.

Keisuke Mukai, Yasuyuki Ogino, Juro Yagi and Satoshi Konishi, "2-D Evaluation of Bred Tritium Using Neutron Imaging Plate." *IEEE Transactions on Plasma Science*, 2020. 48 no. 6: pp. 1831-1835.

PRESENTATIONS

Yasuyuki Ogino, Shunsuke Kenjo, Toshiro Sakabe, Keisuke Mukai, Mahmoud Bakr, Juro Yagi, and Satoshi Konishi, "Measurements of neutron spatial distribution divided into specific energy regions inside a blanket mock-up." 29th IEEE Symposium on Fusion Engineering (SOFE), 2021. Online.

Yasuyuki Ogino, Keisuke Mukai, Juro Yagi and Satoshi Konishi, "Simulations for practical measurement of spatial neutron distribution inside blanket mock-up irradiated with DT neutrons." 31st Symposium on Fusion Technology (SOFT), 2020. Online.

Yasuyuki Ogino, Keisuke Mukai, Juro Yagi and Satoshi Konishi, "Measurement of the Neutron Distribution with Cylindrical DD neutron Source." 21st US-Japan Workshop on Fusion Neutron Sources and Applications, 2019. Kyoto, Japan.

Yasuyuki Ogino, Keisuke Mukai, Juro Yagi and Satoshi Konishi, "Measurement of Neutron fluence with Removal of X-/gamma-ray Effect from Neutron Imaging Plate." 14th International Symposium on Fusion Nuclear Technology (ISFNT), 2019. Budapest, Hungary.

Yasuyuki Ogino, Keisuke Mukai, Juro Yagi and Satoshi Konishi, "Benchmarking of Neutron Transport in Blanket Module by MCNP with Profile Analysis with Imaging Plate." 23rd Topical Meeting on the Technology of Fusion Energy (TOFE), 2018. Orlando, Florida, USA.

Other 1 proceeding and 6 presentations as co-author.
10 domestic (Japanese) conferences (as co-author included).